UNIVERSITY OF CALIFORNIA, MERCED

Bio-inspired adaptive materials

A dissertation submitted in partial satisfaction of the requirements for the degree of

Doctor of Philosophy

in

Materials and Biomaterials Science and Engineering

by

Bohao Xu

July 2025

Dissertation Committee:

Professor Aleksandr Noy, Chair

Professor Sarah Kurtz

Professor Son Nguyen

Professor Yue (Jessica) Wang, Advisor

SIGNATURE PAGE

The Dissertation of Bohao Xu is approved, and it is acceptable in quality and form for publication on microfilm and electronically:

_____

Professor Aleksandr Noy, Chair and Committee Member

_____

Professor Sarah Kurtz, Committee Member

_____

Professor Son Nguyen, Committee Member

_____

Professor Yue (Jessica) Wang, Advisor and Committee Member

Table of contents

Acknowledgement

First and foremost, I would like to express my deepest gratitude to my advisor, Dr. Yue (Jessica) Wang, whose guidance, patience, and insight shaped every stage of this dissertation. Your support and expectations have challenged me to grow as a real PhD who always thinks deeply about things. Your mentorship has been far more than academic; it has shaped my perspective of seeing this world. I started appreciating and enjoying nature more than ever.

I am also grateful to my committee members—Dr. Sarah Kurtz, Dr. Aleksandr Noy, and Dr. Son Nguyen—for their valuable feedback, encouragement, and thoughtful questions throughout my PhD journey.

I would like to thank my lab mates, Dr. Ian Hill, Victor Hernandez, Celeste Castillo, Dr. Di Wu, Leonela Gutierrez, and Emily Tran, for their kind help in this work. I am also very grateful to other lab mates for making the lab a place of learning, energy, and support. A big thank you to our collaborators, Dr. Michael Yeung and Abe Rosenberg at the University at Albany, Ruhao Li from Stevens Institute of Technology, for their help on TGA. Special thanks to Kennedy Nguyen at the UC Merced Imaging and Microscopy Facility (IMF) for his expert guidance and technical support. Your support made the imaging work in the lab not only productive but enjoyable.

I am grateful to the Army Research Office and UC Merced ORED Seed Grant Program for providing the financial and infrastructural support that made this research possible.

I am deeply grateful to the coaches and teammates at Merced MMA for being a steady source of discipline, resilience, and community throughout my PhD journey. Professor Marcos Tome and Professor Mauricio Tome made this gym more than a training space—but more like a harbor to heal, a home to rest. Thank you for the hard rounds of sparring! You helped me stay physically and mentally tough. I would also like to thank Dr. Ian Hill for his kindness and generosity in helping me improve my wrestling. That made me confident to start a grappling game with my opponents.

I would like to sincerely thank Haiyan Wang, Xuyuan Zhao, Mike Nawrocki, Alex Perl, Bob Deklinski, and Eric Zhao from Sierra Academy of Aeronautics for their generosity in allowing me to use their cafeteria and stay in the dormitory during a challenging period of my PhD journey. This provides great convenience for me to work at our Castle lab. In the meantime, I would also like to thank the UC Merced Pavilion for consistently providing affordable, clean, and nutritious food throughout my time as a graduate student.

To my former housemates, Dr. Miaomiao Liu and Dr. Weifeng Gao—thank you for your companionship, laughter, and kind advice in everything!

Lastly, and most importantly, I thank my parents and my wife for their unwavering understanding and support throughout this journey. Thank you for allowing me the freedom to pursue what I truly love, even when it meant long hours, uncertainty, and distance. Your trust, patience, and quiet strength gave me the space to grow—not just as a researcher, but as a person. This work would not have been possible without your love.

Thank you all!

CURRICULUM VITAE

EDUCATION

- **University of California, Merced**

Expected in August 2025 Ph.D., Materials and Biomaterials Science and Engineering (MBSE)

Merced, CA

- **Zhengzhou University**

M.Sc., Packaging Materials and Engineering

Zhengzhou, China

- **Fujian Agricultural and Forestry University**

B.Sc., Materials Science and Engineering

Fuzhou, China

RESEARCH EXPERIENCE

University of California, Merced

2020 -2025

Graduate student, Advisor: Prof. Yue (Jessica) Wang

Developing adaptive and transformative electronic materials that mimic the mechanical properties of living matter

Advanced Bio-Inspired Adaptive and Transformable Mold

- Developing advanced DLP printing combined with injection molding methods, using adaptive molds that can expand or shrink to accommodate different infill sizes. This approach enables high-resolution 3D printing of challenging materials.

Adaptive "J-Shape" Behavior Replication for Advanced Electronics or Armors

-Developed a magnetorheological fluid (MRF) composite method to replicate human skin's "J-shape" behavior, reducing mechanical mismatch in next-generation stretchable and wearable electronics.

Mechanically Transformative and Adaptive Materials

-Developed a bioinspired transformative material that integrates a nacre-mimic “brick-and-mortar” structure, enabling temperature-driven soft-hard transitions with enhanced toughness in the stiff state.

University of California, Merced

2018 - 2020

Graduate student, Advisor: Prof. Jennifer Lu

Fabrication of hierarchical electrodes with high gravimetric capacitance.

National Institute for Materials Science, Japan

July - October 2017 Intern student, Advisor: Dr. Takeo Minari

Thermoplastic polyurethane as the charge-trapping layer for flexible OTFTs with wider memory windows.

Zhengzhou University, China

2015 - 2018

Master student, Advisor: Prof. Jinzhou Chen

-Aligned functional graphene to achieve anisotropic mechanical properties using the thermo-compression technique.

-Investigated and optimized directional mechanical performance, i.e., in-plane stretching, out-of-plane bending.

-Demonstrated potential applications in flexible electronics and advanced structural materials.

HONORS AND AWARDS

- **UC Merced RED SEED Grant Recipients** *(2023)*: Grant supporting early-stage research, fostering innovation, and enhancing external grant competitiveness.
- **UC Merced Summer MBSE Bobcat Fellowship** *(2019, 2021, 2022, 2023)*
- **UC Merced MBSE Best Elevator Speeches** *(2022)*: Recognizes graduate students in MBSE for delivering the most concise, impactful research presentations.

PUBLICATIONS

- **Xu, B.**, Wu, D., Li, R., Wang, Y. "3D-Printed thermal stable superabsorbent template for conductive materials" (In preparation)
- **Xu, B.**, Wang, Y. "Self-protective behaviors of intelligent and adaptive magnetorheological composites" (In preparation)
- **Xu, B.**, Gutierrez, L., Hernandez, V., Wang, Y. "Bioinspired tough and mechanically transformative materials" (In preparation)
- **Xu, B.**, Wu, D., Hill, I. M., Halim, M., Rubin, Y., Wang, Y. (2023). "A new and versatile template towards vertically oriented nanopillars and nanotubes." Nanoscale Advances, 5(17), 4489-4498.
- Hill, I. M.*, Hernandez, V.*, **Xu, B.***, Piceno, J. A., Misiaszek, J., Giglio, A.,…Wang, Y. (2023). "Imparting High Conductivity to 3D Printed PEDOT: PSS." ACS Applied Polymer Materials, 5(6), 3989–3998.*Co-first authors.
- Hill, I. M., **Xu, B.**, Rosenberg, A. A., Chang, J., Wu, D., Rice, W., Tran, E., Gutierrez, L., Rubin, Y., Yeung, M. T., Wang, Y. "3D-Printing Assisted Casting of Pure PEDOT with Complex Architectures." (In preparation)
- Hill, I. M., Wu, D., **Xu, B.**, Wang, Y. (2023). "Oligoaniline-assisted self-assembly of polyaniline crystals." Materials Horizons, 10(4), 1282-1291.
- Hernandez, V., Jordan, R. S., Hill, I. M., **Xu, B.**, Zhai, C., Wu, D., ... Wang, Y. (2023). "Deformation rate-adaptive conducting polymers and composites." Small, 2207100.
- Jordan, R., Frye, J., Hernandez, V., . . .**Xu, B.**, Hill, I. M., Wang, Y. (2021). "3D printed architected conducting polymer hydrogels." Journal of Materials Chemistry B, 9(35):7258-7270.
- Ding, C., **Xu, B.**, Zhang, J., Sun, Q., Chen, Z., Liu, S., ... Chen, J. (2021). "Chitosan wrapped graphene/polyurethane composites with improved dielectric properties for capacitive sensing." Polymer Science, Series A, 63(5), 576-584.
- **Xu, B.**, Yang, H., Dai, K., Liu, X., Zhang, L., Wang, M., ... Chen, J. (2018). "Thermo-compression-aligned functional graphene showing anisotropic response to in-plane stretching and out-of-plane bending." Journal of Materials Science, 53(9), 6574-6585.

CONFERENCE PRESENTATIONS AND INVITED TALKS

- **Xu, B.**, "Transformative magnetorheological systems", Invited Guest Talk for the course "Structure and Properties of Materials." April 11, 2024, UC Merced.
- **Xu, B.**, Gutierrez, L., Wang, Y. "Bioinspired tough and mechanically transformative materials." Oral Presentation. American Chemistry Society (ACS) Meeting. March 17–21, 2024, New Orleans, Louisiana, USA.
- **Xu, B.**, Hernandez, V., Wang, Y. "Mechanically transformative electronic materials." Poster Presentation. American Chemistry Society (ACS) Meeting. August 21–25, 2022, Chicago, Illinois, USA.

TEACHING EXPERIENCE

- **Introduction to Cognitive Science**

2020 Spring
Teaching assistant to Prof. Paul Smaldino
Leading student discussions on the topic of learning, evolution, vision and attention, languages, social and cultural cognition, and consciousness.

- **Introduction to Materials Science**
  2019 Spring, Fall
  Teaching assistant to Prof. Svetla Gargova
  Review quiz and homework problems/solutions, facilitated student laboratory experiments.

SKILLS

- **Material synthesis and processing:** graphene surface modification (arching small molecules), polymer and resin chemistry (formulation of custom 3D printing resins), polymer hot press molding, interfacial polymerization (synthesis of polyurea and polyurethane shell microcapsules), electroplating, electropolymerization, direct ink write (DIW), and digital light processing (DLP) 3D printing
- **Material characterizations:** FT-IR, SEM, AFM, XRD, TGA, DSC, rheometer, electrochemical characterization, tensile testing (Instron), electrical testing (Keithley)
- **Cleanroom device fabrication:** CVD, various inkjet-printing techniques
- **CAD:** Rhinoceros 3D, Autodesk Inventor, Autodesk Fusion 360, Autodesk 3ds Max
- **Programming Languages:** C/C++

LEADERSHIP AND VOLUNTEER EXPERIENCE

- **Lab Procurement Specialist** *(2023 – Present) Prof. Yue (Jessica) Wang's lab*
- **Lab Safety Officer** *(2021 – Present) Prof. Yue (Jessica) Wang's lab*
- **Core Leader,** *"Imagine It, Build It!" 3D Printing Workshop (Summer 2021 UC Merced CalTeach Program)*

PROFESSIONAL DEVELOPMENT AND CERTIFICATIONS

- Smarter, Not Harder: AI productivity Workshop, UC Merced, *onsite 2025*
- Introduction to Semiconductor Packaging, Arizona State University, *online 2024*
- Semiconductor Packaging Manufacturing, Arizona State University, *online 2024*
- Advanced Semiconductor Packaging, Arizona State University, *online 2024*

ABSTRACT

Adaptive materials that could dynamically change their material properties in response to diverse environments have attracted intensive attention in recent years. The adaptive behaviors of this new kind of material addressed the limitations of traditional manufactured materials that only have static properties, thus making it suitable for next-generation electronics, robotics, and armor. However, there are still limited numbers of synthetic adaptive materials. In this work, three independent projects will be discussed, each of which used living organisms in nature as inspiration to replicate adaptive behaviors within synthetic materials. In the first project, we imbued bioinspired transformative materials of sea cucumbers with a second bioinspired property—toughening of the stiff state through a nacre-mimic "brick" and "mortar" structure. "Soft-hard" transition behaviors can be readily induced upon the trigger of temperature as a stimulus. In the "Hard" state, the nacre-inspired "brick" and mortar" structure exhibited improved toughness. In the second project, we were intrigued by the "J-shape" strain-stress behaviors of human skin. Therefore, we used a new methodology that harnesses the squeeze behavior of magnetorheological fluid (MRF) to achieve reproduction of the "J-shape" behaviors. The as-prepared bioinspired material showed adaptive "J-shape" mechanical responses. And our study further proved that the "J-shape" curve could be tuned by segmentation and manual activation of designed MRF pockets. In our final project, we set pufferfish as an example to mimic the "bulking" behaviors of pufferfish and prepared an adaptive and transformable mold that allows for dynamic infill size control. Collectively, my PhD work has advanced the understanding and devised new strategies to replicate adaptive behaviors of living organisms in "life-like" synthetic materials, thus enriching the library of bio-inspired adaptive materials and providing new avenues to next-generation intelligent matter.

Chapter 1
Overview of bio-inspired adaptive materials

1.1 Move forward from responsive material to adaptive materials

Stimuli-responsive materials have been great examples of "Smart" materials for many years. Those materials are responsive to single physical or chemical stimuli (e.g., light, current, pH, specific chemicals), and change between state A and state B (Figure 1.1 (a)). The transition could be reversible when counter stimuli are applied to this system.[1] Responsive materials overcome the limits of traditional materials that have fixed material properties, endowing materials with bistable behaviors in relation to the environment.

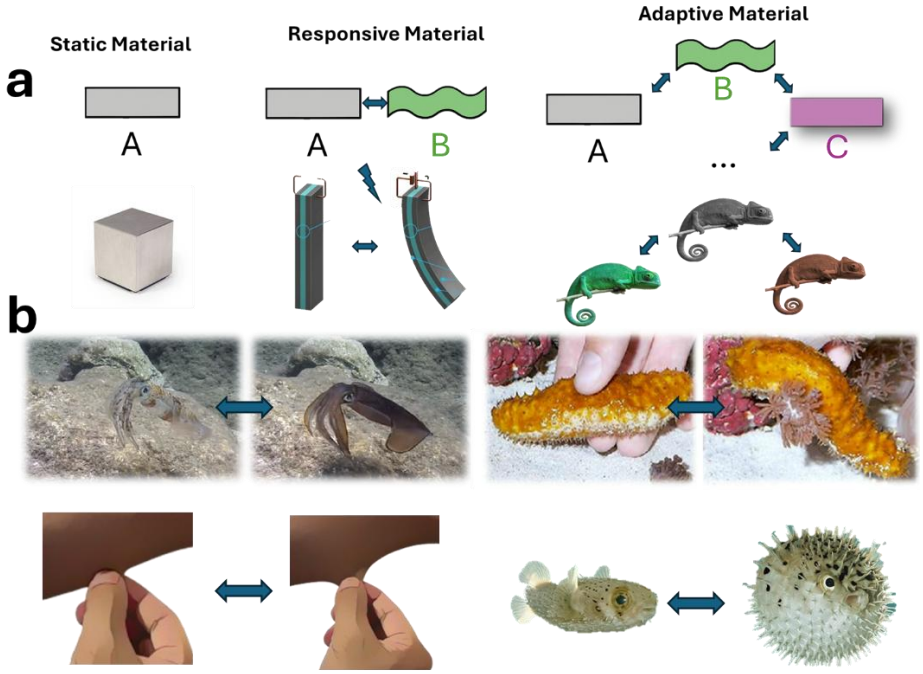

Figure 1.1 (a) Illustration of static material, responsive material, and adaptive material, (b) Examples of adaptive behaviors in nature. Top left: color change of cephalopods; top right: stiffness changes of sea cucumbers; bottom left: "J-shape" behavior of human skin; bottom right: "bulking" of pufferfish.

With the development of artificial intelligence and soft robotics, people are looking for even "smarter" materials that can satisfy various applications of different scenarios within one sole material. This material will be not solely responsive but also **adaptive** to the environment. A call for adaptive material shortly draws people's attention. In 2019, Andreas Walther[2] first distinguished adaptive material from responsive material from the energy landscape perspective. He described the classic responsive system as a switch between two low-energy states upon a trigger. Repetitive trigger or operation makes no difference to this system. As a more complex system, an adaptive system could have more than two states, and the response to the same trigger may change over time. This requires material systems to be more "life-like" living matter in nature.

1.2 Adaptive materials developed by nature

Throughout the long history of evolution and adaptation, living creatures have developed millions of strategies to adjust themselves to fast-changing living conditions and surroundings to survive. As a result, numerous examples of adaptive materials developed by living organisms have been observed. Here, we selected a few common examples to represent different types of adaptive materials.

Cephalopods are known for their dynamically controlled adaptive camouflage.[3] (Figure 1.1 (b)). Cephalopods have the ability to hide themselves in the background by matching the surrounding patterning, color, shape, and texture. Leucophores, iridophores, and chromatophores are found to be three essential active cells to achieve color change in cephalopods' skin.[4] The chromatophores serve as filters that absorb/transmit light. The chromatophore organs are directly controlled by neurons, which helps to achieve rapid color change.

Other than the color change, sea cucumbers developed the ability to change the stiffness of their body(Figure 1.1 (b)).[5,6] They could either be in a "soft" state so that they can squeeze themselves into a narrow channel to hide from their enemies, or switch to a "hard" state to protect themselves from razor-toothed predators.[7] The span of modulus change is estimated to vary from 5 MPa to 50 MPa[8]. This "soft-hard" dynamic switch is neurally controlled by interactions between adjacent collagen fibers. This type of transient interaction is usually triggered within a few seconds after the neurotransmitter is secreted.

Similar to sea cucumber, our human skin is also a delicate example of adaptive materials that dynamically adjust the mechanical properties (Figure 1.1 (b)). If we pulled our skin from our arm, we would not feel much resistance at first. However, after reaching a certain point, it becomes dramatically difficult to pull the skin further. This is characterized as "J-shape" strain-stress behaviors.[9] Many soft biomaterials, like skin, though very thin and flexible, toughen themselves by exhibiting a "J-shape" strain-stress behavior as a self-protection mechanism against excessive deformation. This mechanical behavior is described as a small stress increase under low-strain deformation in the initial stage, with a dramatic stress growth under a further large strain deformation till failure. This mechanism is rooted in the conformation of curved and entangled collagen fibers. Once the tensile strain is applied, the fibers initially de-curl or detangle, resulting in a negligible stress increase. The stress quickly increases after the collagen is straightened, thus initiating the breaking of the polymer chains.[9]

Instead of changing the stiffness, pufferfish developed survival skills to control their size when detecting dangers (Figure 1.1 (b)).[10] They could quickly inflate themselves by swallowing a large amount of water or air to deter predators. During inflation, a significant amount of water is captured by the mouth and is stored in an expandable stomach. The unwanted water was later pumped out by a "coughing" behavior to return to their original sizes. Similarly, plants developed this kind of size control adaptability with the help of water as well. Resurrection plants, or Selaginella lepidophylla, curl into a small ball under low humidity to minimize water evaporation.[11] But they open up and expand in size when water is available. This adaptive change in size allows them to survive in extremely dry conditions for years.

1.3 Bio-inspired materials: learning from nature

Bioinspiration is a process to appreciate the beauty of nature's exquisite design and utilizes existing examples in nature as guidance for synthetic materials. Learning from nature offers human beings a "shortcut" for innovations. This route has three key merits: 1) Nature offers inexhaustible solutions and ideas. Although the exact number may not be accurately counted, scientists estimate

there are several million species co-existing with us on the planet at present. Each species, even the simplest one, requires dozens of interdependent systems, thus offering tons of references for engineering materials 2) All inspirations have been "carefully" filtered by natural selection. Throughout the long history of evolution and adaptation, nature conducted millions of "experiments" to determine which optimized design is best suited for survival. It accumulated a giant database where each dataset had been reproduced thousands of times in each generation. Those datasets enable us to save a great amount of time and effort in exploring the best engineering design. 3) Solutions offered by nature are usually sustainable and environmentally friendly. Unlike synthetic materials, natural materials are usually made of renewable, biodegradable ingredients. The growing process does not always come with high temperatures, high pressures, or other demanding conditions. Most of the biomaterials are considered green and eco-friendly.

The fabrication of bioinspired synthetic materials could be achieved through two routes: 1) directly mimicking the design principles. A classic, well-known example is borrowing the design rules from the lotus leaf, which has micro-protrusions and nano-hairs on its surface[12] to increase the contact angle to repel water droplets. As a result, water droplets would ball up, roll across the leaf surface, and carry dirt particles away. Synthetic materials with these structural features successfully replicate the same superhydrophobic properties, making the materials self-cleaning.[13] Other examples include the lessons from the hook structure of burrs to create the first Velcro and gecko feet-inspired adhesive. For the latter, a surface with hair-like microscopic structures, similar to the setae of gecko feet, was designed to maximize the van der Waals force and contact area with the opposite surface (Figure 1.3). [14] 2) Mimic the multifunctionality of natural materials but achieve the same functions through different strategies. A stark contrast is that some synthetic materials do not necessarily follow the same structural design of the lotus leaf, but alter the property of the material by surface coating[15] to replicate the same superhydrophobic properties. Another example is the cephalopod-inspired camouflage materials that adopt electrically[16] or thermally[17] responsive material to change color in response to stimuli, instead of using muscle or pigment cells.

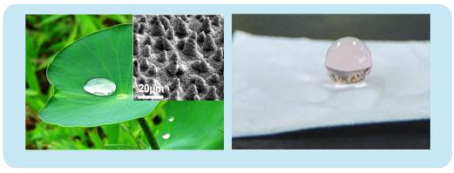

Lotus leaf-inspired superhydrophobic material

Bur-inspired fastener

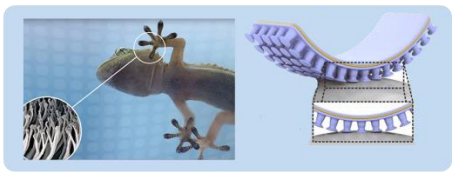

Gecko feet-inspired adhesive surface

Figure 1.3 Examples of directly mimicking the design principles of living materials.

Considering the above-mentioned successful examples of bioinspired materials led us to wonder whether bioinspiration could contribute to the manufacture of next-generation adaptive materials, which typically require higher complexity in functions and pose greater challenges in preparation.

1.4 Bio-inspired adaptive material

Harnessing inspirations from biomaterials to fabricate adaptive materials has been explored by several groups. Here, I list four types of synthetic adaptive materials that mimic functions or behaviors of living matter. Three of them served as inspirations for my PhD research, which is described in the subsequent chapters.

1.4.1 The "Soft-hard" transition of sea cucumber

Based on the type of stimulus, replication methods could be categorized into four groups (Figure 1.4.1). 1) Temperature-stimulated "soft-hard" transitional materials were explored by harnessing the melting temperature of liquid metals,[18] manipulating the glass transition temperatures of polymers,[19,20] 2) Chemical-stimulated materials, for example, the sea cucumber itself, are a perfect example of regulating their body stiffness by the construction/destruction of collagen fiber networks. This change is triggered by "messages" delivered by secreted neurotransmitters. Other systems were created by using impurity,[21] inorganic salts,[22] and organic crosslinker[23] as the stimuli to initialize the phase change of the corresponding responsive matrices. 3) Field-stimulated materials such as electrorheological fluid,[24] magnetorheological fluid,[25] and shear-thickening fluid[26] are used as active matter to tune the properties of the composites with the help of physical fields. 4) Structural design could also be applied to achieve the transition. Printed interconnected armor was prepared. Upon jamming, two layers of interlocked granular particle fabrics compress each other, thereby stiffening the composite.[27]

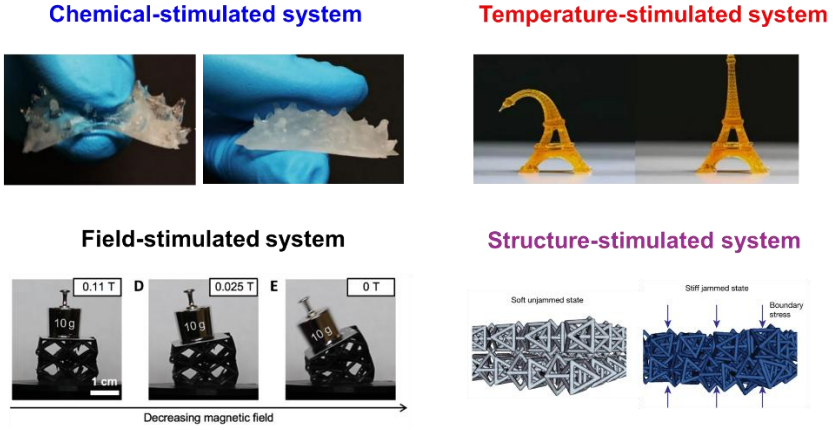

Figure 1.4.1 Synthetic "Soft-hard" transition materials.

1.4.2 "J-shape" material

2D patterning typically embeds a flat 2D thin film in a pattern of wavy, horseshoe, or triangular shapes onto or into a flexible matrix. Upon stretching, the curled pattern resembles the process of straightening curled collagens, therefore generating an adaptive resistance. For example, Zhalmuratova et al.[28] sandwiched fabrics between silicone elastomer layers to get a fabric-reinforced elastomer composite. Their materials offer strain-stiffening and anisotropic mechanical properties that closely replicate the "strain-stiffening" of the human aorta. Zhang et al.[29] used a similar sandwich structure to embed aramid fibers with a curvy pattern inside a polyurethane matrix to mimic the gular sac tissue of the brown pelicans. Materials exclusively based on textiles could also be viewed as another type of 2D patterning.[30] Studies have shown that the external force has to first uncoil the looped and interconnected knit, then straighten the yarns, which also mimics the biomaterial case. 3D structural engineering could be seen as an advancement of 2D patterning. The increased dimension gives the whole structure more freedom to preserve the hidden length or

volume of the materials. Typical methods involve employing designs like origami[31] or kirigami[32] to fold extra volume and release it during the stiffening stage. Other 3D structures like helical[9] or octet[33] also have extra length; therefore, materials undergo a "releasing" period before stiffening.

1.4.3 Pufferfish material

Adaptive size and shape control have been successfully achieved by structure-programmed shape memory polymer[19,34] or field-responsive materials.[24,35] The former mostly relies on the synthesis of a polymer with the desired glass transition temperature. Upon heating or cooling, the softened/hardened polymer will deform or relax to its original shape. Researchers designed and 3D-printed those polymers into a "flower" shape to achieve the "bloom" and "close-up".[36] The latter used a similar route where field-responsive material was printed into a 3D structure. The material is triggered by the "on/off" of applied fields (such as electric fields and magnetic fields). The active matter inside the matrix will change the orientation to align better with the field, thus leading to the folding of the whole structure.

1.5 Chapter outlines

My PhD focused on developing adaptive and transformative materials that mimic the mechanical properties of living matter. My goals are to replicate dynamic and adaptive functions that exist in living organisms in synthetic materials. The outline of my three independent projects is summarized below.

Mechanically Transformative and Adaptive Materials (Chapter 2)

-Inspired by the sea cucumber and nacre examples, we proposed combining features of sea cucumber and nacre into a single entity. We explored and offered a solution to endow transformative materials with high toughness by building them in a complex "brick and mortar" structure.
-We prepared a material that could serve as an active layer for transformative electronics or multifunctional robots.

Adaptive "J-Shape" Behavior Replication for Advanced Electronics or Armors (Chapter 3)

-We developed a new methodology to replicate the "J-shape" mechanical behavior found in human skin using magnetorheological fluid (MRF) composites.
-This work addressed the mechanical mismatch in next-generation stretchable and wearable electronics, offering potential advancements in wearable devices and future armor applications.

Advanced DLP Printing with High-Temperature Molds for Expanded Material Compatibility (Chapter 4)

-Inspired by the dynamic size control of pufferfish, we conceived the idea of creating an adaptive and transformable hydrogel mold using the superabsorbent material.
-Mimicking such behaviors and applying this principle to DLP-printed molds enables modulation of infill volumes and expands the material limitations for high-resolution 3D printing.
-This method provided a thermal stability mold, enabling broader applications with polymer, metal-containing composites, and pure metal in additive manufacturing.

1.6 References

(1) Kang, S. H. Dynamically Adaptive Materials. *MRS Bull.* **2024**, *49* (11), 1121–1126. https://doi.org/10.1557/s43577-024-00798-3.

(2) Walther, A. Viewpoint: From Responsive to Adaptive and Interactive Materials and Materials Systems: A Roadmap. *Adv. Mater.* **2020**, *32* (20), 1905111. https://doi.org/10.1002/adma.201905111.

(3) Hanlon, R. Cephalopod Dynamic Camouflage. *Curr. Biol.* **2007**, *17* (11), R400–R404. https://doi.org/10.1016/j.cub.2007.03.034.

(4) Phan, L.; Kautz, R.; Leung, E. M.; Naughton, K. L.; Van Dyke, Y.; Gorodetsky, A. A. Dynamic Materials Inspired by Cephalopods. *Chem. Mater.* **2016**, *28* (19), 6804–6816. https://doi.org/10.1021/acs.chemmater.6b01532.

(5) Bellamkonda, R. V. Marine Inspiration. *Nat. Mater.* **2008**, *7* (5), 347–348. https://doi.org/10.1038/nmat2176.

(6) Scott, A. R. Secrets from the Deep Sea. *Chem. Eng. News* **2004**, *82* (16), 26–32.

(7) Khan, A. *Adapt: How Humans Are Tapping into Nature's Secrets to Design and Build a Better Future: How Humans Are Tapping into Nature's Secrets to Design and Build a Better Future*; St. Martin's Publishing Group, 2017.

(8) Capadona, J. R.; Shanmuganathan, K.; Tyler, D. J.; Rowan, S. J.; Weder, C. Stimuli-Responsive Polymer Nanocomposites Inspired by the Sea Cucumber Dermis. *Science* **2008**, *319* (5868), 1370–1374. https://doi.org/10.1126/science.1153307.

(9) Ma, Y.; Feng, X.; Rogers, J. A.; Huang, Y.; Zhang, Y. Design and Application of 'J-Shaped' Stress–Strain Behavior in Stretchable Electronics: A Review. *Lab. Chip* **2017**, *17* (10), 1689–1704. https://doi.org/10.1039/C7LC00289K.

(10) Wainwright, P. C.; Turingan, R. G. Evolution of Pufferfish Inflation Behavior. *Evolution* **1997**, *51* (2), 506–518. https://doi.org/10.1111/j.1558-5646.1997.tb02438.x.

(11) Brulé, V.; Rafsanjani, A.; Asgari, M.; Western, T. L.; Pasini, D. Three-Dimensional Functional Gradients Direct Stem Curling in the Resurrection Plant *Selaginella Lepidophylla*. *J. R. Soc. Interface* **2019**, *16* (159), 20190454. https://doi.org/10.1098/rsif.2019.0454.

(12) Balani, K.; Batista, R. G.; Lahiri, D.; Agarwal, A. The Hydrophobicity of a Lotus Leaf: A Nanomechanical and Computational Approach. *Nanotechnology* **2009**, *20* (30), 305707. https://doi.org/10.1088/0957-4484/20/30/305707.

(13) Zhang, X.; Ding, B.; Cheng, R.; Dixon, S. C.; Lu, Y. Computational Intelligence-Assisted Understanding of Nature-Inspired Superhydrophobic Behavior. *Adv. Sci.* **2018**, *5* (1), 1700520. https://doi.org/10.1002/advs.201700520.

(14) Kizilkan, E.; Strueben, J.; Staubitz, A.; Gorb, S. N. Bioinspired Photocontrollable Microstructured Transport Device. *Sci. Robot.* **2017**, *2* (2), eaak9454. https://doi.org/10.1126/scirobotics.aak9454.

(15) Golovin, K.; Boban, M.; Mabry, J. M.; Tuteja, A. Designing Self-Healing Superhydrophobic Surfaces with Exceptional Mechanical Durability. *ACS Appl. Mater. Interfaces* **2017**, *9* (12), 11212–11223. https://doi.org/10.1021/acsami.6b15491.

(16) Wang, Q.; Gossweiler, G. R.; Craig, S. L.; Zhao, X. Cephalopod-Inspired Design of Electro-Mechano-Chemically Responsive Elastomers for on-Demand Fluorescent Patterning. *Nat. Commun.* **2014**, *5* (1), 4899. https://doi.org/10.1038/ncomms5899.
(17) Ke, Y.; Zhang, Q.; Wang, T.; Wang, S.; Li, N.; Lin, G.; Liu, X.; Dai, Z.; Yan, J.; Yin, J.; Magdassi, S.; Zhao, D.; Long, Y. Cephalopod-Inspired Versatile Design Based on Plasmonic VO2 Nanoparticle for Energy-Efficient Mechano-Thermochromic Windows. *Nano Energy* **2020**, *73*, 104785. https://doi.org/10.1016/j.nanoen.2020.104785.
(18) Byun, S.-H.; Sim, J. Y.; Zhou, Z.; Lee, J.; Qazi, R.; Walicki, M. C.; Parker, K. E.; Haney, M. P.; Choi, S. H.; Shon, A.; Gereau, G. B.; Bilbily, J.; Li, S.; Liu, Y.; Yeo, W.-H.; McCall, J. G.; Xiao, J.; Jeong, J.-W. Mechanically Transformative Electronics, Sensors, and Implantable Devices. *Sci. Adv.* **2019**, *5* (11), eaay0418. https://doi.org/10.1126/sciadv.aay0418.
(19) Ge, Q.; Sakhaei, A. H.; Lee, H.; Dunn, C. K.; Fang, N. X.; Dunn, M. L. Multimaterial 4D Printing with Tailorable Shape Memory Polymers. *Sci. Rep.* **2016**, *6* (1), 31110. https://doi.org/10.1038/srep31110.
(20) Gong, X.; Xie, F.; Liu, L.; Liu, Y.; Leng, J. Electro-Active Variable-Stiffness Corrugated Structure Based on Shape-Memory Polymer Composite. *Polymers* **2020**, *12* (2), 387. https://doi.org/10.3390/polym12020387.
(21) Yang, F.; Cholewinski, A.; Yu, L.; Rivers, G.; Zhao, B. A Hybrid Material That Reversibly Switches between Two Stable Solid States. *Nat. Mater.* **2019**, *18* (8), 874–882. https://doi.org/10.1038/s41563-019-0434-0.
(22) Hsieh, C.-T.; Hsu, S. Double-Network Polyurethane-Gelatin Hydrogel with Tunable Modulus for High-Resolution 3D Bioprinting. *ACS Appl. Mater. Interfaces* **2019**, *11* (36), 32746–32757. https://doi.org/10.1021/acsami.9b10784.
(23) Buchberger, A.; Saini, H.; Eliato, K. R.; Zare, A.; Merkley, R.; Xu, Y.; Bernal, J.; Ros, R.; Nikkhah, M.; Stephanopoulos, N. Reversible Control of Gelatin Hydrogel Stiffness by Using DNA Crosslinkers. *ChemBioChem* **2021**, *22* (10), 1755–1760. https://doi.org/10.1002/cbic.202100030.
(24) Pan, Y.; Liu, X.-J.; Zhao, H. Stretchable and Conformable Variable Stiffness Device through an Electrorheological Fluid. *Soft Matter* **2022**, 10.1039.D2SM01362B. https://doi.org/10.1039/D2SM01362B.
(25) Testa, P.; Style, R. W.; Cui, J.; Donnelly, C.; Borisova, E.; Derlet, P. M.; Dufresne, E. R.; Heyderman, L. J. Magnetically Addressable Shape-Memory and Stiffening in a Composite Elastomer. *Adv. Mater.* **2019**, *31* (29), 1900561. https://doi.org/10.1002/adma.201900561.
(26) Zhang, X.; Wang, P.; Kurkin, A.; Chen, Q.; Gong, X.; Zhang, Z.; Yang, E.-H.; Yang, J. Mechanical Response of Shear Thickening Fluid Filled Composite Subjected to Different Strain Rates. *Int. J. Mech. Sci.* **2021**, *196*, 106304. https://doi.org/10.1016/j.ijmecsci.2021.106304.
(27) Wang, Y.; Li, L.; Hofmann, D.; Andrade, J. E.; Daraio, C. Structured Fabrics with Tunable Mechanical Properties. *Nature* **2021**, *596* (7871), 238–243. https://doi.org/10.1038/s41586-021-03698-7.
(28) Zhalmuratova, D.; La, T.-G.; Yu, K. T.-T.; Szojka, A. R. A.; Andrews, S. H. J.; Adesida, A. B.; Kim, C.; Nobes, D. S.; Freed, D. H.; Chung, H.-J. Mimicking "J-

Shaped" and Anisotropic Stress–Strain Behavior of Human and Porcine Aorta by Fabric-Reinforced Elastomer Composites. *ACS Appl. Mater. Interfaces* **2019**, *11* (36), 33323–33335. https://doi.org/10.1021/acsami.9b10524.
(29) Zhang, H.; Shu, J.; Liu, Z.; Wu, J. High-Performance Crack-Resistant Elastomer with Tunable "J-Shaped" Stress–Strain Behavior Inspired by the Brown Pelican. *ACS Appl. Mater. Interfaces* **2022**, *14* (19), 22489–22496. https://doi.org/10.1021/acsami.2c06646.
(30) Maziz, A.; Concas, A.; Khaldi, A.; Stålhand, J.; Persson, N.-K.; Jager, E. W. H. Knitting and Weaving Artificial Muscles. *Sci. Adv.* **2017**, *3* (1), e1600327. https://doi.org/10.1126/sciadv.1600327.
(31) Filipov, E. T.; Paulino, G. H.; Tachi, T. Origami Tubes with Reconfigurable Polygonal Cross-Sections. *Proc. R. Soc. A.* **2016**, *472* (2185), 20150607. https://doi.org/10.1098/rspa.2015.0607.
(32) Isobe, M.; Okumura, K. Initial Rigid Response and Softening Transition of Highly Stretchable Kirigami Sheet Materials. *Sci. Rep.* **2016**, *6* (1), 24758. https://doi.org/10.1038/srep24758.
(33) Hanif, A.; Yoo, D.; Kim, D.; Mustafayev, F.; Hajiyev, S.; Kim, D. S. Recent Progress in Strain-Engineered Stretchable Constructs. *Int. J. Precis. Eng. Manuf.-Green Technol.* **2024**, *11* (4), 1403–1433. https://doi.org/10.1007/s40684-023-00565-w.
(34) Luo, L.; Zhang, F.; Wang, L.; Liu, Y.; Leng, J. Recent Advances in Shape Memory Polymers: Multifunctional Materials, Multiscale Structures, and Applications. *Adv. Funct. Mater.* **2024**, *34* (14), 2312036. https://doi.org/10.1002/adfm.202312036.
(35) Kim, Y.; Yuk, H.; Zhao, R.; Chester, S. A.; Zhao, X. Printing Ferromagnetic Domains for Untethered Fast-Transforming Soft Materials. *Nature* **2018**, *558* (7709), 274–279. https://doi.org/10.1038/s41586-018-0185-0.
(36) Hu, X.; Zhou, J.; Vatankhah-Varnosfaderani, M.; Daniel, W. F. M.; Li, Q.; Zhushma, A. P.; Dobrynin, A. V.; Sheiko, S. S. Programming Temporal Shapeshifting. *Nat. Commun.* **2016**, *7* (1), 12919. https://doi.org/10.1038/ncomms12919.

Chapter 2
Bio-inspired Tough and Mechanically Transformative Materials

2.1 Abstract

Nature has provided a library of inspiration for synthetic materials. Transformative materials may mimic a sea cucumber to switch between low and high stiffnesses, but they lack high toughness to resist brittle fracture. In contrast, bioinspired structural materials usually feature high toughness but cannot transform their shape. The synergistic combination of these two complementary biomimetic features could lead to the creation of advanced transformative electronics. Therefore, in this work, I explored and offered a way to prepare a bioinspired transformative material with a second bioinspired property—toughening of the stiff state through a nacre-mimic "brick and mortar" structure. I employed vat photopolymerization-based 3D printing to fabricate a "brick and mortar" structure with the soft polymer framework as the "mortar", followed by the infiltration of a phase changing material, polyethylene glycol, into the cavities as "bricks". Soft-hard transformative behaviors can be readily induced in these composites using temperature as a stimulus. In the "Hard" state, the nacre-inspired "brick and mortar" structure provides significant toughening with a toughness of 3×10^{-2} MJ/m^3 compared to pure "brick" or pure "mortar". The effects of "brick" dimensions on the toughness of the "Hard" state are systematically investigated.

2.2 Introduction

During the long process of evolution, living organisms developed the adaptability of dynamically changing the stiffness of their bodies to suit their environments better. For example, sea cucumbers evolved to survive by adopting an adaptive behavior that could either loosen their body texture to be in a "Soft" state, so they could squeeze themselves into very narrow channels to hide them away from enemies; or they could swiftly harden their body to switch to a "Hard" state so that they may survive from their razor-toothed predator's mouth.[1–3] This adaptive behavioral trait is a desirable feature for next-generation electronics because conventional, rigid, and stiff circuits and soft, wearable electronics have been mutually exclusive so far. Therefore, it is crucial to synthesize adaptive materials to cater to the needs of making transformative electronics. Several works have been done in recent years to mimic the adaptive behaviors of sea cucumbers. Temperature-stimulated materials were explored by harnessing the melting temperature of liquid metals,[4] manipulating the glass transition temperatures of polymers,[5,6] or adding supercooled chemicals.[7] The sea cucumber itself is a perfect example of chemically stimulated materials. Sea cucumbers can regulate their body stiffness by the construction/deconstruction of the collagen fiber network. The change is triggered by "messages" delivered by secreted neurotransmitters. Other systems were created by using impurities,[7] inorganic salts,[8] and organic crosslinker[9] as the stimuli to initialize the phase change of the corresponding responsive matrices. Field-stimulated materials, such as electrorheological fluid,[10] magnetorheological fluid,[11] and shear-thickening fluid[12] have been used as active matter to tune the properties of the composites with the presence of physical fields. Those advancements bring variety to the transformative material library; however, a key fundamental aspect has been neglected. Transformative electronics require high toughness for durability considerations in real applications. Turning from the "Soft" to the "Hard" state, the material is no longer soft and deformable to allow itself to undergo sizable deformation to alleviate the stress. Thus, the transformative material under the "Hard" state calls for high toughness, which is not always accompanied by its regained rigidity.

In stark contrast to the low toughness of most transformative materials, some bioinspired structural materials display high toughness. The components of those materials were assembled in complex hierarchical architectures, which greatly toughened the composites. Notable examples include, but are not limited to, bones,[13] bamboo,[14] and spider silk.[15] Among all those biological structural materials, nacre has been extensively investigated due to its high fracture energy, which is almost 2000 times greater than its building blocks, aragonite plates, commonly considered a brittle material.[13,15] A series of investigations reveals that nacre has multiple toughening mechanisms.[13,16,17] Crack deflection, facilitated by plate interlocking and mineral bridging, was found to be the primary contributor to toughness at the sub-micrometer level.[17] The 10-50 nm organic layer between "bricks" was found to be responsible for the viscoplastic energy dissipation. It also plays a role in crack bridging between "bricks".[16] Nano-asperities on the surface of the "bricks" also increase the sliding resistance and consequently contribute to the increased toughness.[13] Though high toughness may be scored, the majority of the components of those biopsied structural materials are rigid and stiff ceramics. They are generally vulnerable to shape changes and deformation, which emphasizes the importance of reconfigurability and transformability to satisfy the demands of various scenarios encountered in the day-to-day use of next-generation electronics.

I wondered whether I could go beyond simply mimicking existing biological materials or organisms and unify multiple attractive mechanical properties into a single material through rational design. Inspired by the examples mentioned above, I proposed to combine the transformability of sea cucumber with the high toughness of nacre in a 3D structure. Here, we present an approach to achieve this goal. The combined properties were obtained by using transformative material to substitute the stiff "bricks" to construct nacre-like structures. The transformative "bricks" supply tunable stiffness and reconfigurability to the composites, while the complex nacre-inspired structure provides significant toughening effects to the "Hard" state of the composites. The transformative material is able to be stimulated by temperature change and switched between "Hard" and "Soft" states with an "on/off" stiffness ratio of 34. Upon the "Soft" and "Hard" transition, this material could be reprogrammed into multiple shapes and exhibit different levels of load-bearing abilities. This structurally toughened material can serve not only as a transformative platform but also as an impact-buffer layer for integrated electronics in the "Hard" state. The obtained transformative electronic also exhibits good repeatability and recyclability, as the transformative "bricks" could be repaired by melting and re-solidifying, and it remains durable for at least 10 breaking-repairing cycles.

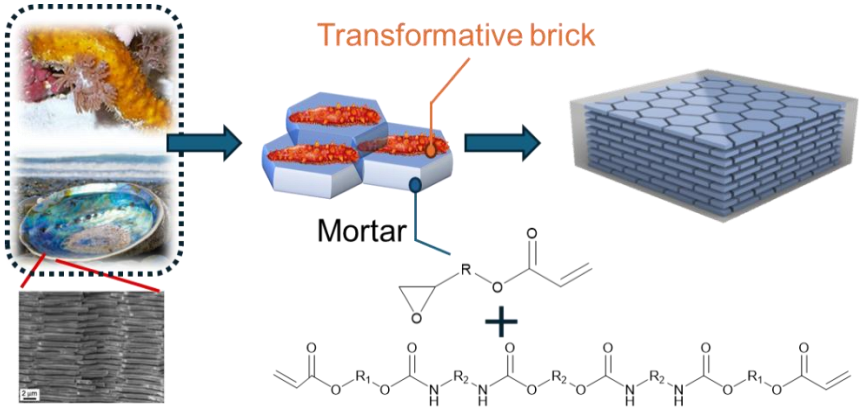

Figure 2.2 Schematic diagram of combining transformative behaviors with high toughness. (Images were from the Reference[18] and Gettyimages[19])

2.3 Material preparation and characterization

2.3.1 "Mortar" and "brick" material selections

The "mortar" layer has been found to be heavily involved in toughening mechanisms of the materials, such as crack deflection, organic bridging, and pull-out of plates.[13] Therefore, materials need to be rationally selected. The "mortar" layer is expected to be soft and stretchable, allowing it to accommodate the stress transferred from the "bricks". A study done by Patel et al.[20] reported a highly stretchable and 3D printable elastomer. The 3D printable characteristics allow the elastomer to be created into a well-defined structure. Inspired by that work, I adopted the same materials of Ebecryl 8413, Allnex, and Ebecryl 113, Allnex; but decreased the ratio from 1:1 to 1: 0.2 to make the "mortar" layer softer to better contact with the "brick" material. For tensile properties, please see Figure 2.3.1 (a) and (b). A photoinitiator, diphenyl(2,4,6-trimethylbenzoyl)phosphine (TPO) (2 wt.%, Tokyo Chemical Industry Co., LTD), was added to the prepared resin. The mixture was probe sonicated for 7 minutes at 40% amplitude until the TPO was fully dissolved in the resin. An organic phase change material, polyethylene glycol 1500 (Sigma-Aldrich), was selected as the "brick" material due to its merits of lightweight, low cost, low melting temperature (~40°C), and relatively fast crystallization rate.

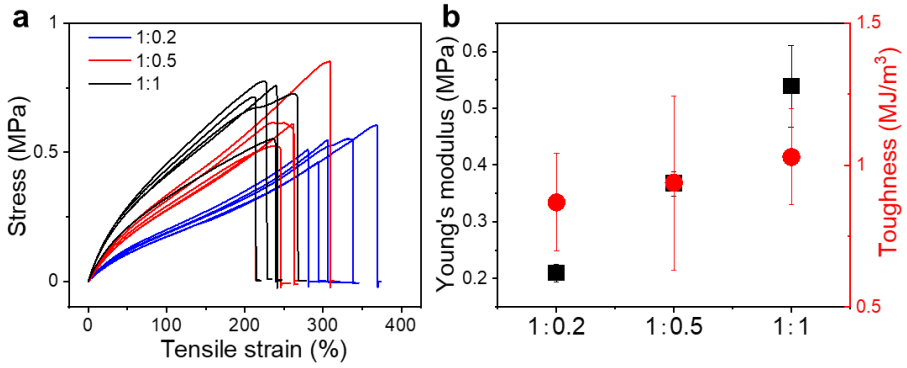

Figure 2.3.1 (a) Tensile stress-strain curves of pure "mortar" layer of three compositions. (Allnex 113: Allnex 8413) (b) Young's modulus and toughness comparison between the same resin compositions.

2.3.2 Fabrication process

The fabrication process consists of three major steps (Figure 2.3.2). The first step was to use Digital Light Processing (DLP) to print the continuous "mortar" structure with the cavities for "bricks". The "mortar" structure was CAD-designed on Autodesk Inventor. The outside "mortar" layers of all samples are 1 mm thick, while the inside layer within the structure has a thickness of 0.5 mm. For overlapping exploration samples, all samples have four layers of "bricks", and each layer has a dozen 15 mm×15 mm×2 mm "bricks". Diameter exploration samples also have four layers, but the "brick" size is 10 mm×10 mm×2 mm, 15 mm×15 mm×2 mm, and 20 mm×20 mm×2 mm, respectively. The 8-layer sample is simply doubling the 4-layer 15 mm×15 mm×2 mm sample in layers. VlareSlicer was used to slice all 3D-drawn structures. Structures were printed on a Masked Stereolithography Apparatus 3D printer (Peopoly Phenom Forge). After a series of optimizations of the printing parameters, the exposure time for each layer was set to 12.00 seconds

with a layer thickness of 50 μm. After printing, samples were washed in isopropanol for 5 minutes and post-cured under UV light for 3 minutes.

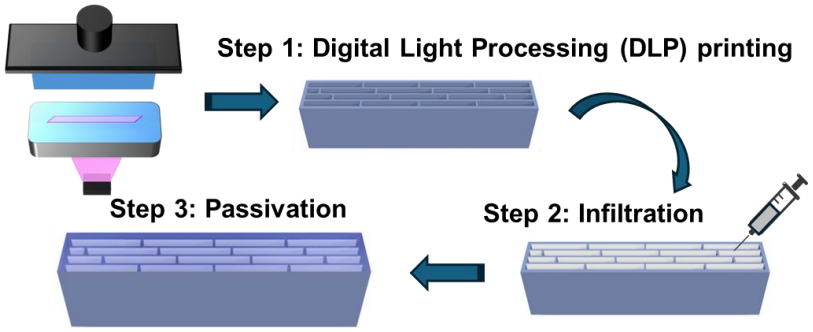

Figure 2.3.2 Nacre-like material preparation process.

The second step is the infiltration of PEG "brick" material. Melted PEG 1500 was then injected into the top-open "mortar" structure through a syringe. After the "bricks" were injected, I let them cool until the PEG was solidified, and then followed the third step by casting and curing the resin as the top layer (~ 1 mm in thickness).

2.3.3 Mechanical and Electrical Testing

A 3-point bending test was done on Instron 3369 with a load cell of 100 N. A constant 10 mm/min bending rate was applied to all samples. Deflections and load values were recorded by the machine. The deflection to strain and load to stress conversion was calculated according to the following formula[21]:

$$\sigma = \frac{3FL}{2bd^2} \; ; \varepsilon = \frac{6gd}{L^2}$$

where σ is the flexural stress at the midpoint, (MPa); F is the load at a given point on the load-deflection curve, (N); L is the length of support span, (mm); b and d are the width of test beam, (mm) and the depth or thickness of tested beam, (mm) respectively. ε is the flexural strain in the outer surface, (mm/mm); g = maximum deflection of the center of the beam, (mm).

For toughness, the single-edge notched measurement technique did not work well for my all-polymer samples, as the polymers are very tolerant of stress, but once a crack was formed, it quickly went to failure. For that reason, I calculated the toughness by integrating the area of stress-strain curves.

The configuration of the conductive device is shown in Figure 2.3.3 (a). A copper foil with one side adhesive was attached to the surface of the "brick and mortar" sample. Electrical measurements were done by clamping the electrodes on the extended left and right copper foils. The resistance of the copper foil on the "brick and mortar" sample under bending was measured using a Keithley 2450 sourcemeter.

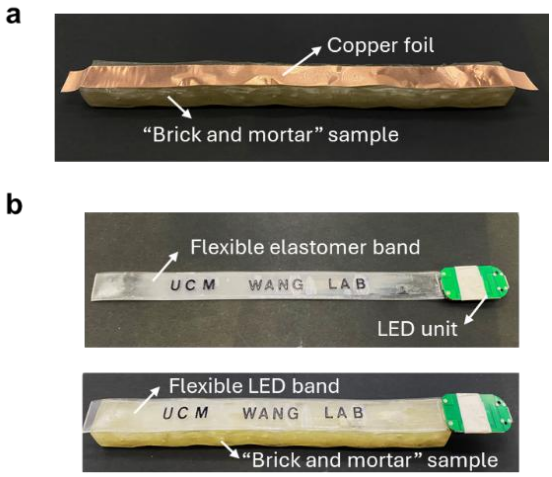

Figure 2.3.3 Configuration of devices (a) Conductive copper foil integrated with "brick and mortar" sample. (b) Flexible LED band integrated with "brick and mortar" sample

The illuminating device was obtained by integrating a flexible LED band on the "brick and mortar" sample (Figure 2.3.3 (b)). I peeled off the original plastic shell of the band, leaving only the LED unit and the elastomer band. The flexible LED device was adhered to the "brick and mortar" sample with double-sided tape.

2.4 Transformative behaviors of "brick and mortar" materials

The transformative "brick" PEG 1500 I selected has a melting point of around 40℃. Therefore, at an elevated temperature of 60℃, my material could be completely melted into a near-liquid state ("Soft" state) and switch back to an all-solid-state ("Hard" state) after cooling. I selected the 15 mm×15 mm "brick" size sample as a demonstration to illustrate the transformative behaviors. The bending modulus of the "Soft" state sample could be as low as 490 kPa while the modulus of the "Hard" state reaches 9.23 MPa (Figure 2.4.1 (a) and (b)), the "on/off" ratio of this sample is 19 which is higher than that of sea cucumber (around 10).[22] The high "on/off" ratio benefits from the soft "mortar" layer I selected, and it is possible for me to tune the composition to make a softer "mortar" to increase that value further. However, we will witness a lower toughness as the "mortar" becomes more fragile. A potential way to further tune the "on/off" ratio is to adopt different "brick" materials. In Figure 2.4.1 (c), I chose PEG 600, PEG 1500, and PEG 10,000, which have similar molecular structures but different stiffnesses, as examples to demonstrate that the "Hard" state stiffness could be improved. Here, I only used materials from the PEG family; however, the "brick" material selection is not limited to organic compounds; ceramics or metals may also be used, based on the needs of real applications. The material also witnessed a dramatic change in toughness during the transition. From the "Soft" state to the "Hard" state, the toughness climbs from 4.3×10^{-4} MJ/m^3 to 3×10^{-2} MJ/m^3. This almost 70 times toughness difference is evidence that stiff "brick" material is a key part in toughening the material.

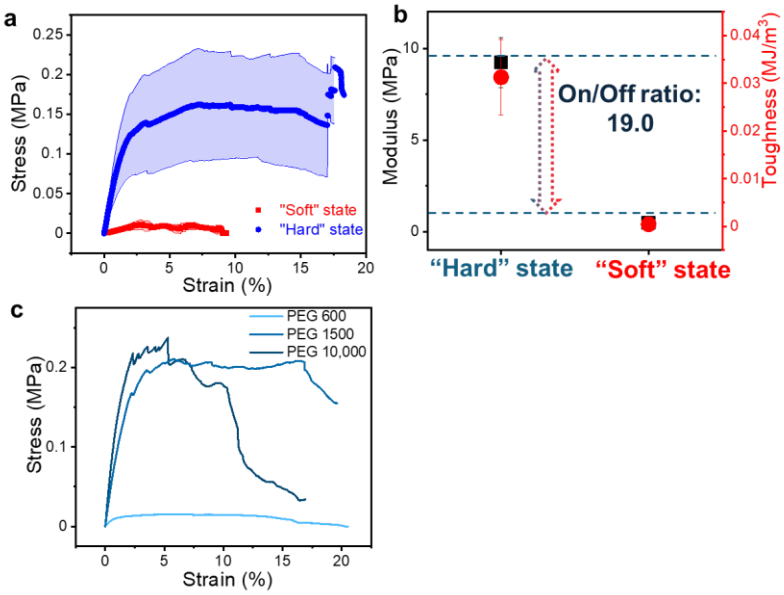

Figure 2.4.1 (a) Bending stress-stain curves of "Soft" and "Hard" state samples. (b) Mechanical properties comparison between "Soft" and "Hard" state nacre-like samples. (c) Bending stress-strain curves of PEG 600, PEG 1500, and PEG 10, 000 with a "brick" size of 15 mm.

Upon the "Soft/Hard" transition, this material exhibits different load-bearing abilities (Figure 2.4.2 (a)). Under the "Hard" state, the material is stiff enough to hold a 100 g weight between an overhang, but is so soft that it couldn't support that weight after being switched to the "Soft" state. The sample quickly sagged down and dropped the weight. Because of the characteristics of the "Soft/Hard" transition, I am able to reconfigure the sample into different shapes under the "Soft" state and lock that shape by switching back to the "Hard" state. Therefore, the prepared samples have good reconfigurability. To illustrate this, I melted the sample and then programmed it into a letter. After being cooled to be resolidified, the letter remains in that shape permanently till I re-melt it. I present letters of "U", "C", and "M" in sequence in Figure 2.4.2 (b).

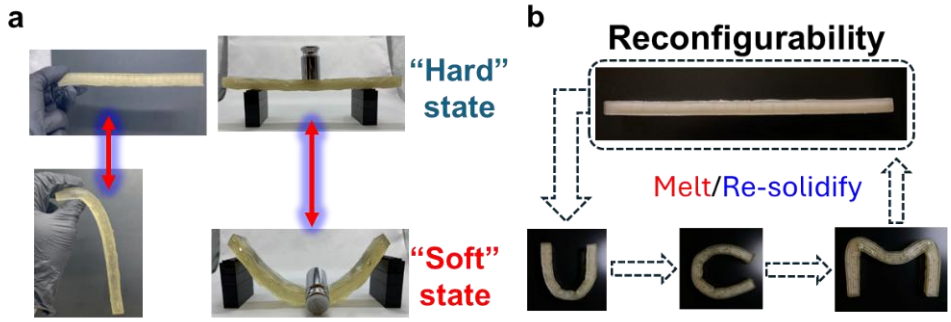

Figure 2.4.2 (a) Transformative behaviors between "Hard" and "Soft" states, and the load-bearing ability difference between "Hard" and "Soft" states. (b) Reconfigurability of the nacre-like sample. The sample has been shaped into "UCM" separately.

The "Soft/Hard" transition not only brings the material with good reconfigurability but also endows the sample with repairable characteristics. To demonstrate this, I repeatedly performed

breaking-repairing for 10 cycles (Figure 2.4.3 (a)). Specifically, I bent the sample to a 15 mm extension (~5% strain), which is a safe value that breaks some of the "bricks" but won't cause too much damage to the material. Then, the sample was heated in an oven at 60°C to melt the "bricks". After re-solidification, the broken pieces of the "bricks" rejoined together. All the samples exhibit good repeatability, such that the load-deflection curves overlap almost perfectly among the 10 cycles. In the meantime, I adhered a copper foil on the top side of the "brick and mortar" sample to repeat the 10 bending cycles. The recorded resistance shows that the bending process has a minimal effect on the electrical performance, as the R/R_0 value remains consistently at 1 ± 0.1 after connections were stabilized. This means that it may be safe to integrate electrical devices with the "brick and mortar" material, as the nacre-like structure prevents the crack from damaging the devices. I subsequently selected an LED band to represent flexible electronics and attached it to the "brick and mortar" sample. Under the "Soft" state, the band could be bent and twisted together with the platform and still function well with illumination (Figure 2.4.3 (b)). This demonstrates that this material can serve as a reliable platform for other flexible electronics.

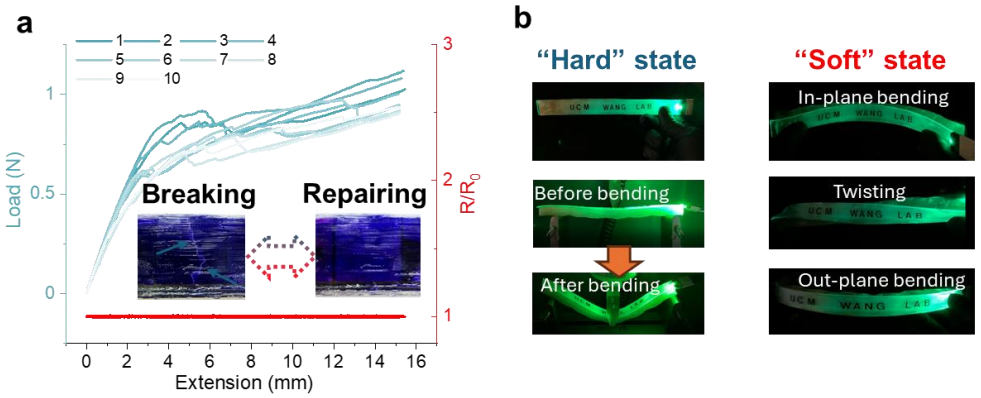

Figure 2.4.3 (a) Breaking-repairing abilities of nacre-like sample (10 cycles). (b) Nacre-like sample integrated with electronics under "Hard" states bending and "Soft" states twisting.

2.5 Enhanced toughness of "brick and mortar" materials

To examine the toughening effect, I prepared four-layered "brick and mortar" samples (with a 15 mm×15 mm×2 mm "brick" size) for testing. As a control, pure "brick" material PEG 1500 and pure "mortar" bars were made for comparison. Three-point bending tests were performed on all those samples. The results are shown in Figure 2.5 (a)-(c). The nacre-like structure does help to combine the stretchability of pure "mortar" with the high stiffness of pure "bricks" in this composite: the "brick and mortar" sample has the same level elongation at break (18.0%) as the pure "mortar" (19.5%) which is a stark contrast to PEG 1500 (1.23%) but is 50 times stiffer than pure "mortar" due to the stiffening contribution from the PEG 1500. Therefore, the obtained "brick and mortar" sample witnesses the highest toughness, which is several times higher than that of pure "mortar" and pure "bricks". It should be mentioned that the toughness value here is not strikingly high due to the use of low-molecular-weight PEG and soft "mortar" layer. My primary focus here is to provide an exemplary model to show how the nacre-like structure serves both as a complex toughening structure and also as a bridge to mediate the modulus between stiff and soft materials. I anticipate that higher molecular PEGs could also be applied to this structure to get further toughened materials.

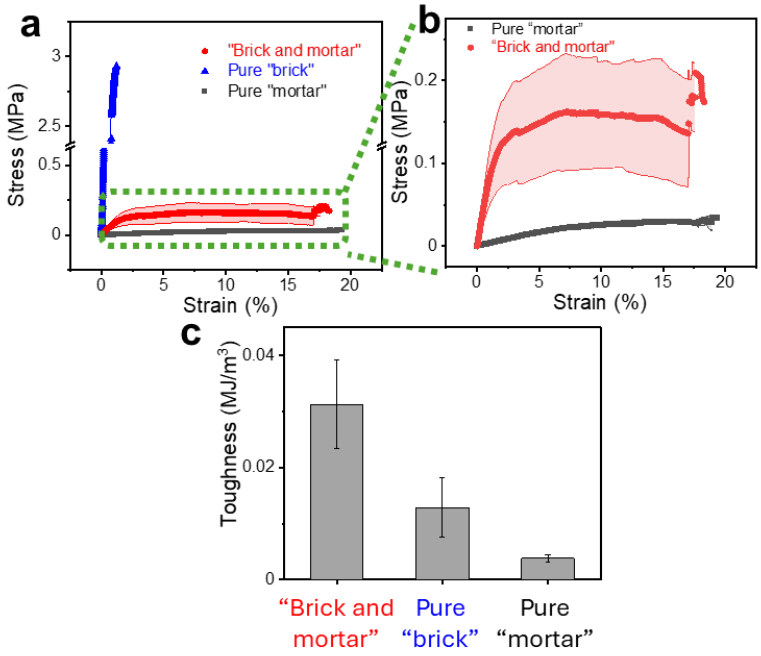

Figure 2.5 (a) and (b) Bending stress-strain curves of "Hard" state nacre-like sample, pure "bricks", and "mortar". (c) Bending toughness comparison between nacre-like samples, pure "bricks", and "mortar" under the "Hard" state.

With the enhanced toughness, upon elevated temperature, the "brick and mortar" sample exhibits the transformative behaviors that it could switch from a stiff "Hard" state to a liquid-like "Soft" state (Figure 2.4.2 (a)). This result proves that the transformative materials could be effectively combined within the "brick and mortar" toughening structure.

2.6 Understanding the toughness enhancement of "brick and mortar" materials

2.6.1 Mechanisms underlying fracture leading to toughness enhancement

To fully understand how the bioinspired structure toughens the material, I carried out *in-situ* failure analysis by videotaping the entire failure process of the samples during three-point bending load-extension experiments. The failure analysis relates the visible changes in the sample to the mechanical curves, allowing me to explore how the nacre-like pattern impacts crack propagation, thereby extending the toughness. As Figure 2.6.1 (a) and (b) show, the extension of the "brick and mortar" sample is initially linear to the load; no cracks form in this stage. As the upper anvil continues to bend the sample, the slope of the curve starts to change. Microcracks might form inside the PEG "bricks" during this stage; therefore, the curve has a moderate slope. I would consider that as a prelude to the upcoming major crack initiation. When the stress exceeded the limit of the outer "mortar" layer, major cracks started to grow across the "bricks" and "mortar," and samples began to break. Once they formed, these millimeter-sized cracks started to propagate and travel across the sample. Those millimeter-sized cracks could be very detrimental to materials as they will quickly propagate across the sample and cause a catastrophic failure. However, because of the modulus mismatch between the "Hard" and "Soft" phases, the crack shifted its travel direction as it approached the interface. That shift usually causes a crack deflection, which makes the crack penetration more tortuous to proceed. At this stage, I observed stepwise or sawtooth-like load-extension curves. This kind of feature is believed to be the toughened mechanism of nacre.[23,24] Additionally, it should be noted that multiple cracks were observed on each sample (Figure 2.6.1

(b), Point 1 and Point 2). They formed at different times, but they underwent similar initiation and propagation periods till the test ended. I noticed that each time a new major crack formed, it was always followed by a drop in load on the mechanical curve. This suggests that the structure used crack formation as a way to avoid stress concentrated in one place, thus postponing the failure process.

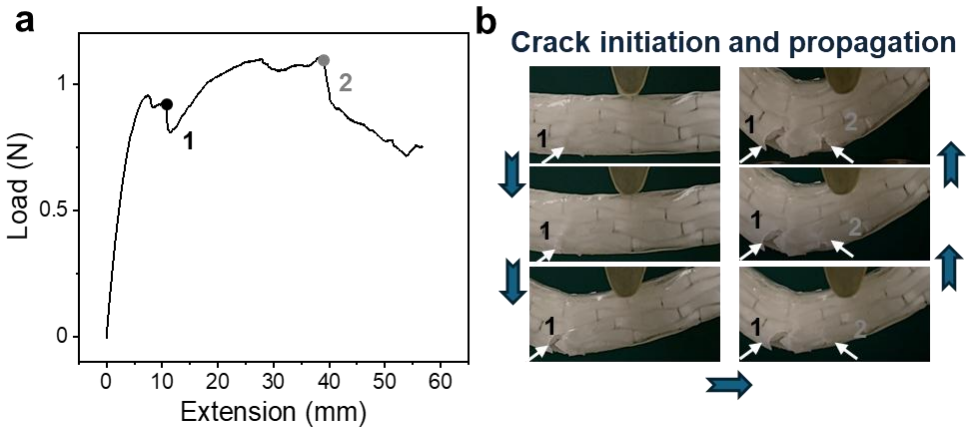

Figure 2.6.1 Bending failure analysis of nacre-like samples. (a) three-point bending load-extension curve. (b) images taken at different stages of the bending process.

In addition to the crack deflection that I observed in the failure process, several other toughening mechanisms were also found (Figure 2.6.2). In my chosen material system, the "mortar" layer is so stretchable that it could stay uncracked and bridge over the crack-penetrated "bricks". The uncracked "mortar" layer partially dissipated the strain energy near the crack tip, thus slowing down the propagation. Constrained microcracking was also observed in my samples, which effectively releases the local stress concentration and is advantageous for the development of crack deflection.[25]

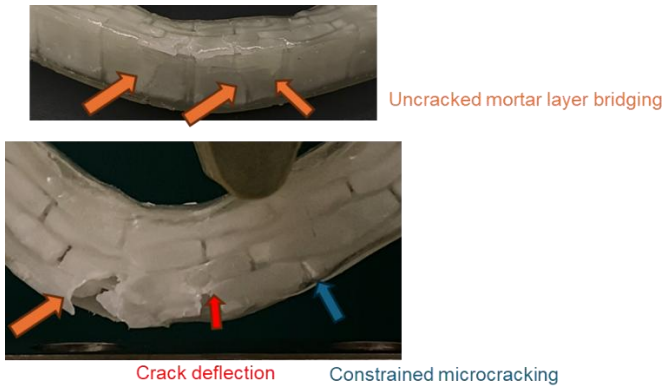

Figure 2.6.2 Images of different toughening mechanisms within one sample.

My previous experiment shows that the nacre-like structure effectively increases the toughness, so a follow-up question is how the structural parameters would influence those results. Based on theoretical predictions from literature and other research papers,[24,26,27] I specifically chose three parameters: the "brick" size, layer numbers, and the overlapping pattern to explore. Other factors may also play a role here, but for practical reasons related to preparation, my exploration will be confined to these three factors.

2.6.2 Structural parameters affecting toughness enhancement

2.6.2.1 Correlation between overlapping pattern and toughness

When "bricks" are "pulling out", they slide over each other, thus creating a resistance to slow down the failure. This resistance is also considered a significant contribution to toughness.[17] I consider the stacking patterns of the "brick and mortar" material as an essential contribution to toughness[28]; therefore, I designed and printed three types of samples. To study the stacking pattern, I define each stacking position as A, B, C, and so on. Each letter represents a slightly different horizontal placement of a layer. Therefore, their stacking arrangement along the Z direction has increasing repeating complexity from ABAB to ABCA, and ABCD (Figure 2.6.2.1.1 (d)). Except for the stacking sequence, all other structural dimensions and material compositions are the same among the three types of samples. The mechanical properties are shown in Figure 2.6.2.1.1 (a) and (b). Those three patterns have almost the same bending modulus around 10 MPa, while that of ABCD is slightly higher than the other two. In terms of toughness, contrary to my prediction that ABCD may have the highest value (the closest pattern to real nacre), ABCA scored the highest, followed by ABCD, and subsequently, ABAB.

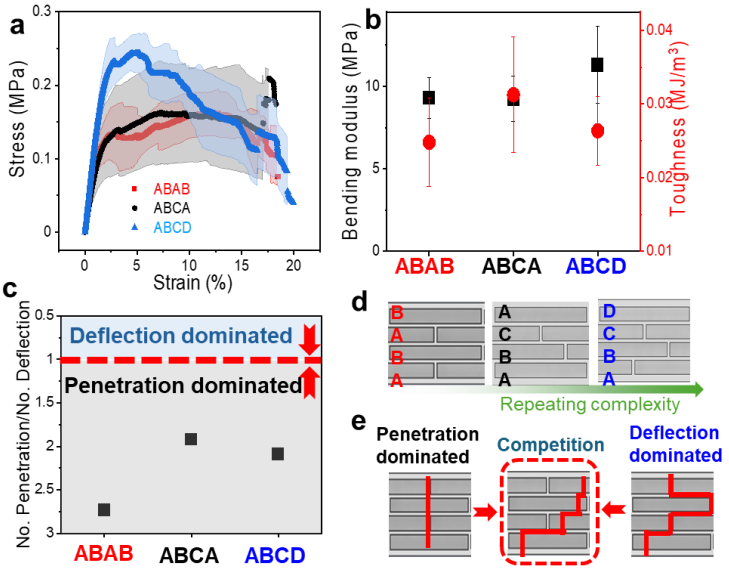

Figure 2.6.2.1.1 Structural parameters optimization of nacre-like samples: stacking pattern exploration. (a) Bending stress-strain of ABAB, ABCA, and ABCD patterns. (b) Bending modulus and toughness comparison of those stacking patterns. (c) Ratios of major penetrations and deflections of ABAB, ABCA, and ABCD patterns. (d) Schematic drawing showing the ABAB, ABCA, and ABCD stacking patterns. (e) A schematic drawing showing the ideal failure mode is a competition between penetration-dominated and deflection-dominated.

I set out to understand how the overlapping pattern influences the toughness, since the underlying insights may lead to a better design of tougher materials. To explore this, I revisited the prerequisites of high toughness. High toughness favors crack growth in a way that has competition between two extreme failure modes[29] (Figure 2.6.2.1.1 (e)). The first extreme is a penetration-dominated mode. That usually happens when the "brick" material is not stiff enough, so the crack breaks the "bricks" in a straight direction with no detours. The short travel path enables the crack to break the material quickly to failure; therefore, the material lacks high toughness. On the opposite side, the other extreme is when the "brick" is too stiff, so the crack can only propagate through the

weak phase (the "mortar" layer). This leads to a deflection-dominated failure mode. Although cracks may take a tortuous path to travel, their route is constrained to the "mortar" layer. Therefore, an ideal case of high-toughness material requires there to be equal numbers of deflections and penetrations to compete with each other. Cracks that propagate within these materials need to travel in a winding manner and may be terminated by stiff "bricks".

Based on that theory, I could determine whether my samples have a fair competition between deflection and penetration by counting the number of crack deflections and penetrations of each sample. As Figure 2.6.2.1.2 shows, "bricks" that have a noticeable crack pathway along the y-axis would be counted as one penetration. If this crack continues to propagate to a second "brick", I will then add the penetration number to two. Similarly, any crack that grows along the x-axis would add to the number of deflections. In my case, I counted double deflection as only one deflection that has two directions. However, in real cases, the crack might not grow perfectly parallel to the axis. So, I decomposed the crack into its respective components on the *x* and *y* axes. Take one sample of the ABCA pattern as an example: three "bricks" were decomposed into components along the y-direction. Therefore, the major penetration number is 3 (indicated by the red arrows). Two "bricks" that have negative or positive *x* components increase (dark blue arrows). Hence, the major deflection number of this sample is 2. By using this method, I counted the number of major deflections and penetrations of each sample (Figure 2.6.2.1.2).

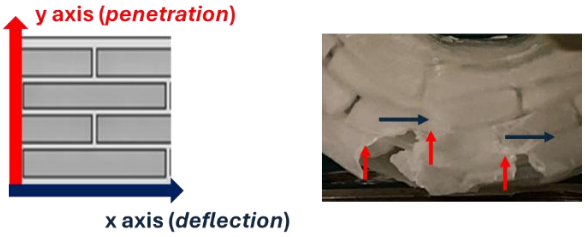

Figure 2.6.2.1.2 Scheme of major penetration and deflection counting method.

Note that I was only able to count the cracks on the edge of the sample, as cracks inside the sample are not easy to observe during the in-situ bending process. The number I got might be lower than the real total number of cracks within the sample. However, it could serve as a qualitative analysis of the competition between penetration and deflection. This value was further compared with results from theoretical parameters. Ratios of deflection and penetration are listed in Table 2.6. Interestingly, the ABCA pattern has the lowest ratio of 1.92, with the ABCD coming as the second, 2.09, followed by 2.73 of ABAB (Figure 2.6.2.1.1 (c)). This trend aligns with the toughness comparison, which suggests that the ABCA pattern has a higher likelihood of experiencing more deflections to compete with the penetration.

Table 2.6 Ratios of major penetration numbers to deflection numbers of each nacre-like sample.

	Stacking pattern		
	ABAB	ABCA	ABCD
Sample 1	(8:4)	(3:2)	(8:2)
Sample 2	(7:0)	(7:6)	(5:1)

Sample 3	(5:2)	(5:3)	(4:2)
Sample 4	(6:2)	(4:1)	(3:3)
Sample 5	(4:3)	(4:0)	(3:3)
Total	(30:11)	(23:12)	(23:11)
Ratio	2.73	1.92	2.09

To further elucidate why ABCA has more deflections than ABCD, I found literature that developed a theoretical parameter, Π_2, to predict the failure mode.[29] They defined $\Pi_2 = 0.5\ t/L$, where t stands for the thickness of the interface; L is the lateral length of the "brick". Since I can assume that all interfaces have the same thickness, this equation tells us that the possibilities of deflections are related to the lateral length of the "brick". However, the lateral length here is no longer equivalent to the "brick" size anymore. The lateral length is now the distance between two vertical "mortar" layers. Based on how differently the "bricks" stack on each other, the lateral length varies, thus giving us different Π_2 values. The Π_2 values of ABCD, ABAB, and ABCA patterns were calculated in Figure 2.6.2.1.3 (a)-(c). The physical meaning of the Π_2 values could be the likelihood that a crack can travel from a "mortar" layer into a different "brick" in a specific geometry. Higher values indicate that a crack has a greater chance of crossing "mortar" or "brick" interfaces. In my current system, ABCA would be the optimized pattern for the highest toughness.

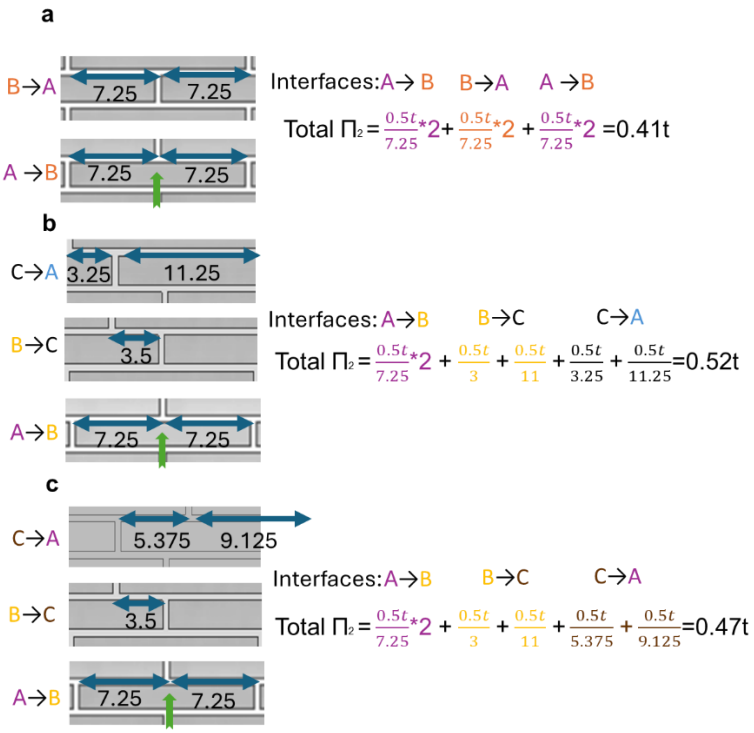

Figure 2.6.2.1.3 Schematic graph showing how the Π_2 values were calculated based on the mechanical interpretation and the calculations of the Π_2 values of each stacking pattern. (a) ABAB. (b)ABCA. (c)ABCD.

2.6.2.2 Correlation between "brick" size and toughness

My next focus is to investigate the correlation of "brick" size with toughness. The increase in "brick" size will lead to an increase in both the aspect ratio and the "brick" volume fraction, both of which could result in a higher modulus. On the one hand, modulus is usually exclusive to toughness, which might lead to a decrease in toughness. On the other hand, stiffer "bricks" will help to dissipate more energy before breaking, thus slowing down the crack growth. This dilemma needs to be experimentally addressed; therefore, I designed three "brick" sizes with "brick" diameters ranging from 10 mm to 15 mm and 20 mm (Figure 2.6.2.2.1 (a)). Except for the "brick" size, all other parameters, including the stacking pattern, remain the same. The aspect ratios of those "bricks" are 5, 7.5, and 10. Accordingly, as a consequence of the change in "brick" size, the "brick" volume fraction also ranged from 55 vol.%, 59 vol.%, to 60 vol.%.

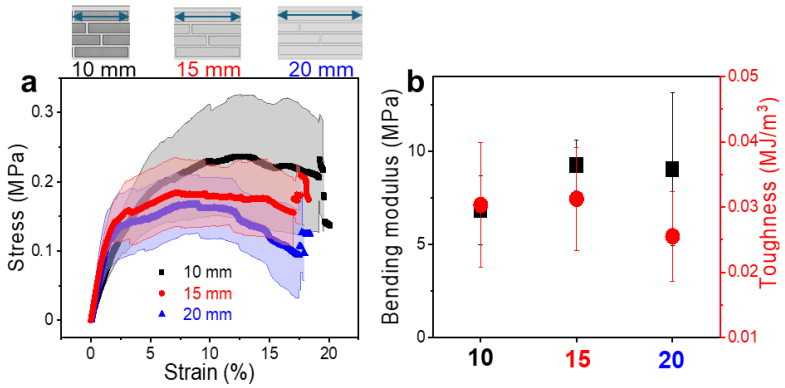

Figure 2.6.2.2.1 Structural parameters optimization of nacre-like samples (a) Bending stress-strain of samples that have 10 mm, 15mm, and 20 mm "brick" size. (b) Bending modulus and toughness comparison between different "brick" sizes.

I conducted the three-point-bending tests on those three types of samples; the results are shown in Figure 2.6.2.2.1 (a). Surprisingly, the 15 mm samples have a higher value than the other two types in terms of both modulus and toughness (Figure 2.6.2.2.1 (b)). I noticed that smaller "bricks" have more vertical "mortar" walls to separate each "brick" in my design. Therefore, the bigger "brick"-size sample may have fewer vertical "mortar" layers inside the structure, working as supports. However, having too many vertical layers may not be ideal. The sample will then likely compromise the entire strength of the composites. To verify my hypothesis, I designed a series of control group samples. I simplified the structure to a single layer. The sample with the largest "brick" size has only one "brick" that is 30 mm×30 mm×2 mm. The second-largest sample was obtained by dividing the largest "brick" into two 15 mm×15 mm×2 mm "bricks" by a vertical 1 mm-thick "mortar" layer. Similarly, the smallest "bricks" were obtained by dividing the largest "brick" into four 7.5 mm×7.5 mm×2 mm "bricks" with three vertical "mortar" layers (Figure 2.6.2.2.1). Because of this special design, samples have zero, one, and three "mortar" walls, respectively. The "mortar" walls only take up 0.68 vol.% and 1.8 vol.% of the whole volume of each sample. Therefore, those are negligible volume increases. Upon the bending test, the 30 mm "brick" without "mortar" walls exhibits a steep slope in the stress-strain curves at the very beginning, indicating that the sample is significantly stiffer than the other two. However, after passing its peak stress, the slope dramatically drops, and the sample becomes softer than the other two from then on. In comparison, samples with one and three "mortar" walls do not exhibit this trend. Instead, they respond linearly with the increased strain, although the 7.5 mm was initially disturbed by a small peak. The "special" tangent modulus change of the 30 mm "brick" sample could be caused by the breakage of the PEG "brick". The optical image in Figure 2.6.2.2.1 clearly shows that a big crack

evenly breaks the "brick". I would relate this breakage to the peak in the stress-strain curve. Once the "brick" is broken, the rest of the bending process primarily involves bending the "mortar" layer with two broken pieces of "brick". In contrast to this process, the "bricks" were barely damaged or remained intact in the other two samples. The "mortar" layer bends with the "brick" and mediates the stress concentration inside the "brick". Interestingly, the tangent modulus of those three samples during the 10~20% strain shows a similar result to my previous bending modulus (Figure 2.6.2.2.2, red region). This control group helps me explain my results that "mortar" walls play a pivotal role; here, they prevent the direct breakage of "bricks". For larger "brick" samples, the lack of necessary support from the "mortar" layer resulted in the PEG breaking in the very early stages. However, having too many vertical layers is always a sign of a high percentage of "mortar". Higher content of soft "mortar" leads to low stiffness and toughness of the "brick and mortar". To put all those together, in my system, the 15 mm would be an optimized "brick" size for both modulus and toughness.

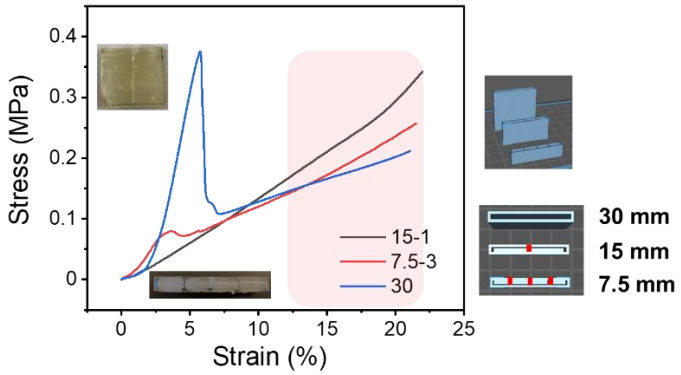

Figure 2.6.2.2.2 Single-layer nacre-like sample bending test, (left): bending stress-strain curve. (right): single-layer sample structure.

I also suspect that PEG 1500 may be a contributing factor to the failure of the 30 mm "brick". To test this, I repeated the experiment with another stiffer material, PEG 10,000, from the same PEG family (Figure 2.6.2.2.3 (a) and (b)). Just as the theoretical prediction suggests that larger "bricks" lead to a higher modulus of the sample, a 30 mm "brick" has a high modulus. But that does not necessarily relate to a high toughness. This result, in turn, proves my previous conclusion that the vertical "mortar" layer is responsible for getting high-toughness material.

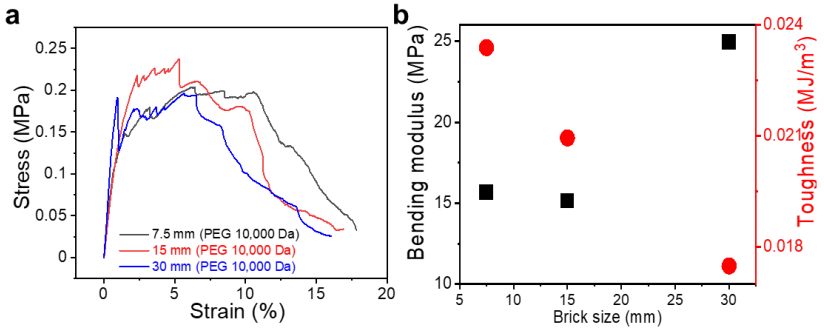

Figure 2.6.2.2.3 (a) Bending stress-strain curves of nacre-like structure with "brick" size of 7.5 mm, 15 mm, and 30 mm (PEG 10, 000). (b) Bending modulus and toughness comparison of different "brick" sizes (PEG 10, 000).

2.6.2.3 Correlation between layer number and toughness

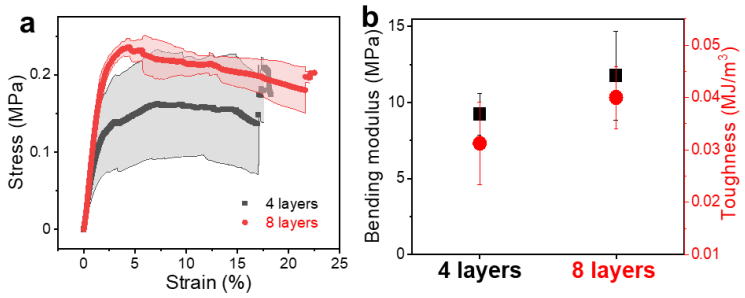

Figure 2.6.2.3.1 (a) Bending stress-strain of four-layer and eight-layer samples. (b) Bending modulus and toughness comparison between four-layer and eight-layer samples.

For simplicity, I designed my sample to have only four layers. However, I still need to understand how the layer number affects the toughness. To investigate that, I doubled the layer number to 8 and performed a bending test. In comparison to the four-layered sample, the eight-layer sample increases the modulus to 11.8 ± 3.0 MPa and the toughness to 0.04 ± 0.006 MJ/m^3 (Figure 2.6.2.3.1 (a) and (b)). According to the *in-situ* failure analysis, no clear crack initiation and propagation were observed within the 8-layered samples (Figure 2.6.2.3.2). The change in the span-to-depth ratio might cause this toughening and stiffening effect. Research has shown that the span-to-depth ratio can lead to a change in bending mode, thereby influencing the mechanical properties.[30] This finding aligns with the natural case: nacre typically consists of thousands of layers to achieve high toughness. For synthetic materials, future designs should favor multiple layers of samples if practical. To maintain simplicity, this work only focused on four-layer samples.

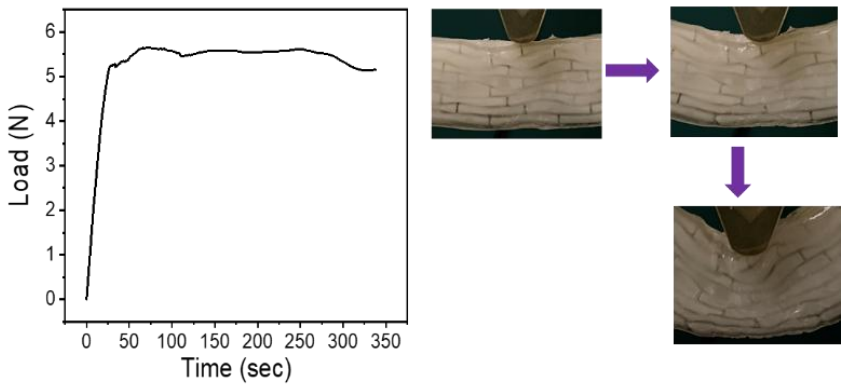

Figure 2.6.2.3.2 Bending failure analysis of eight-layer sample, (left): load-time curve of the bending test. (right): images at different stages.

2.7 Conclusions

I demonstrated a bio-inspired material that combines transformative behaviors with enhanced toughness under the “Hard” state. Upon elevated temperatures, transformative “bricks” were melted into the liquid to reconfigure the material into different shapes while turning into a “Hard” state after solidification. Improved toughness under the “Hard” state enabled the material to protect integrated appliances, enabling it as a transformative platform for electronics.

My exploration of the structural parameters also provides a few insights into designing such a transformative and tough material. 1) To ensure high toughness, the competition between deflection and penetration is preferred over a repeating complexity. 2) Optimization of "brick" size is preferred to be done for each material system. Current theoretical predictions have failed to consider the stiffness effect of all materials; therefore, different material systems require their own optimized "brick" size values, which can only be determined experimentally. 3) To get high toughness, future materials should have as many layers as possible. Layer numbers influence the bending mode of the sample and thus could toughen and stiffen the material. According to the requirements of real applications, these structural parameters can be tuned to produce future transformative and tough materials with optimized properties.

2.8 References

(1) Bellamkonda, R. V. Marine Inspiration. *Nat. Mater.* **2008**, *7* (5), 347–348. https://doi.org/10.1038/nmat2176.

(2) Scott, A. R. Secrets from the Deep Sea. *Chem. Eng. News* **2004**, *82* (16), 26–32.

(3) Khan, A. *Adapt: How Humans Are Tapping into Nature's Secrets to Design and Build a Better Future: How Humans Are Tapping into Nature's Secrets to Design and Build a Better Future*; St. Martin's Publishing Group, 2017.

(4) Byun, S.-H.; Sim, J. Y.; Zhou, Z.; Lee, J.; Qazi, R.; Walicki, M. C.; Parker, K. E.; Haney, M. P.; Choi, S. H.; Shon, A.; Gereau, G. B.; Bilbily, J.; Li, S.; Liu, Y.; Yeo, W.-H.; McCall, J. G.; Xiao, J.; Jeong, J.-W. Mechanically Transformative Electronics, Sensors, and Implantable Devices. *Sci. Adv.* **2019**, *5* (11), eaay0418. https://doi.org/10.1126/sciadv.aay0418.

(5) Ge, Q.; Sakhaei, A. H.; Lee, H.; Dunn, C. K.; Fang, N. X.; Dunn, M. L. Multimaterial 4D Printing with Tailorable Shape Memory Polymers. *Sci. Rep.* **2016**, *6* (1), 31110. https://doi.org/10.1038/srep31110.

(6) Gong, X.; Xie, F.; Liu, L.; Liu, Y.; Leng, J. Electro-Active Variable-Stiffness Corrugated Structure Based on Shape-Memory Polymer Composite. *Polymers* **2020**, *12* (2), 387. https://doi.org/10.3390/polym12020387.

(7) Yang, F.; Cholewinski, A.; Yu, L.; Rivers, G.; Zhao, B. A Hybrid Material That Reversibly Switches between Two Stable Solid States. *Nat. Mater.* **2019**, *18* (8), 874–882. https://doi.org/10.1038/s41563-019-0434-0.

(8) Hsieh, C.-T.; Hsu, S. Double-Network Polyurethane-Gelatin Hydrogel with Tunable Modulus for High-Resolution 3D Bioprinting. *ACS Appl. Mater. Interfaces* **2019**, *11* (36), 32746–32757. https://doi.org/10.1021/acsami.9b10784.

(9) Buchberger, A.; Saini, H.; Eliato, K. R.; Zare, A.; Merkley, R.; Xu, Y.; Bernal, J.; Ros, R.; Nikkhah, M.; Stephanopoulos, N. Reversible Control of Gelatin Hydrogel Stiffness by Using DNA Crosslinkers. *ChemBioChem* **2021**, *22* (10), 1755–1760. https://doi.org/10.1002/cbic.202100030.

(10) Pan, Y.; Liu, X.-J.; Zhao, H. Stretchable and Conformable Variable Stiffness Device through an Electrorheological Fluid. *Soft Matter* **2022**, 10.1039.D2SM01362B. https://doi.org/10.1039/D2SM01362B.

(11) Testa, P.; Style, R. W.; Cui, J.; Donnelly, C.; Borisova, E.; Derlet, P. M.; Dufresne, E. R.; Heyderman, L. J. Magnetically Addressable Shape-Memory and Stiffening in a

Composite Elastomer. *Adv. Mater.* **2019**, *31* (29), 1900561. https://doi.org/10.1002/adma.201900561.
(12) Zhang, X.; Wang, P.; Kurkin, A.; Chen, Q.; Gong, X.; Zhang, Z.; Yang, E.-H.; Yang, J. Mechanical Response of Shear Thickening Fluid Filled Composite Subjected to Different Strain Rates. *Int. J. Mech. Sci.* **2021**, *196*, 106304. https://doi.org/10.1016/j.ijmecsci.2021.106304.
(13) Wegst, U. G. K.; Bai, H.; Saiz, E.; Tomsia, A. P.; Ritchie, R. O. Bioinspired Structural Materials. *Nat. Mater.* **2015**, *14* (1), 23–36. https://doi.org/10.1038/nmat4089.
(14) Askarinejad, S.; Youssefian, S.; Rahbar, N. Toughening and Strengthening Mechanisms in Bamboo from Atoms to Fibers. In *Handbook of Materials Modeling*; Springer, Cham, 2019; pp 1–29. https://doi.org/10.1007/978-3-319-50257-1_88-1.
(15) Li, X.; Chang, W.-C.; Chao, Y. J.; Wang, R.; Chang, M. Nanoscale Structural and Mechanical Characterization of a Natural Nanocomposite Material: The Shell of Red Abalone. *Nano Lett.* **2004**, *4* (4), 613–617. https://doi.org/10.1021/nl049962k.
(16) Grossman, M.; Pivovarov, D.; Bouville, F.; Dransfeld, C.; Masania, K.; Studart, A. R. Hierarchical Toughening of Nacre-Like Composites. *Adv. Funct. Mater.* **2019**, *29* (9), 1806800. https://doi.org/10.1002/adfm.201806800.
(17) Kakisawa, H.; Sumitomo, T. The Toughening Mechanism of Nacre and Structural Materials Inspired by Nacre. *Sci. Technol. Adv. Mater.* **2011**, *12* (6), 064710. https://doi.org/10.1088/1468-6996/12/6/064710.
(18) Dolui, T.; Natarajan, T. S.; Mukhopadhyay, R.; Wießner, S.; Heinrich, G.; Das, A.; Banerjee, S. S. Stimuli–Responsive Mechanoadaptive Elastomeric Composite Materials: Challenges, Opportunities, and New Approaches. *Adv. Eng. Mater.* **2023**. https://doi.org/10.1002/adem.202300584
(19) *"Beached empty Paua, Perlemoen or Abalone shell showing the...* Getty Images. https://www.gettyimages.com/detail/photo/shiny-nacre-of-paua-shell-abalone-washed-ashore-royalty-free-image/177385896.
(20) Patel, D. K.; Sakhaei, A. H.; Layani, M.; Zhang, B.; Ge, Q.; Magdassi, S. Highly Stretchable and UV Curable Elastomers for Digital Light Processing Based 3D Printing. *Adv. Mater.* **2017**, *29* (15), 1606000. https://doi.org/10.1002/adma.201606000.
(21) ASTM International. *Standard Test Methods for Flexural Properties of Unreinforced and Reinforced Plastics and Electrical Insulating Materials*; ASTM D790; ASTM International: West Conshohocken, PA, 2021. https://www.astm.org/d790.
(22) Capadona, J. R.; Shanmuganathan, K.; Tyler, D. J.; Rowan, S. J.; Weder, C. Stimuli-Responsive Polymer Nanocomposites Inspired by the Sea Cucumber Dermis. *Science* **2008**, *319* (5868), 1370–1374. https://doi.org/10.1126/science.1153307.
(23) Bouville, F.; Maire, E.; Meille, S.; Van de Moortèle, B.; Stevenson, A. J.; Deville, S. Strong, Tough and Stiff Bioinspired Ceramics from Brittle Constituents. *Nat. Mater.* **2014**, *13* (5), 508–514. https://doi.org/10.1038/nmat3915.
(24) Askarinejad, S.; Rahbar, N. Toughening Mechanisms in Bioinspired Multilayered Materials. *J. R. Soc. Interface* **2015**, *12* (102), 20140855. https://doi.org/10.1098/rsif.2014.0855.

(25) Song, J.; Fan, C.; Ma, H.; Liang, L.; Wei, Y. Crack Deflection Occurs by Constrained Microcracking in Nacre. *Acta Mech. Sin.* **2018**, *34* (1), 143–150. https://doi.org/10.1007/s10409-017-0724-1.
(26) Style, R. W.; Tutika, R.; Kim, J. Y.; Bartlett, M. D. Solid–Liquid Composites for Soft Multifunctional Materials. *Adv. Funct. Mater.* **2021**, *31* (1), 2005804. https://doi.org/10.1002/adfm.202005804.
(27) Okumura, K. Strength and Toughness of Biocomposites Consisting of Soft and Hard Elements: A Few Fundamental Models. *MRS Bull.* **2015**, *40* (4), 333–339. https://doi.org/10.1557/mrs.2015.66.
(28) Frølich, S.; Weaver, J. C.; Dean, M. N.; Birkedal, H. Uncovering Nature's Design Strategies through Parametric Modeling, Multi-Material 3D Printing, and Mechanical Testing. *Adv Eng Mater* **2017**, *19* (6), e201600848. https://doi.org/10.1002/adem.201600848.
(29) Paggi, M.; Reinoso, J. Revisiting the Problem of a Crack Impinging on an Interface: A Modeling Framework for the Interaction between the Phase Field Approach for Brittle Fracture and the Interface Cohesive Zone Model. *Comput. Methods Appl. Mech. Eng.* **2017**, *321*, 145–172. https://doi.org/10.1016/j.cma.2017.04.004.
(30) Li, H.; Xu, Y.; Hua, X.; Liu, C.; Tao, J. Bending Failure Mechanism and Flexural Properties of GLARE Laminates with Different Stacking Sequences. *Compos. Struct.* **2018**, *187*, 354–363. https://doi.org/10.1016/j.compstruct.2017.12.068.

Chapter 3
Adaptive Magnetorheological System for "J-Shape" Behavior Replication

3.1 Abstract

"J-shape" strain-stress behaviors have been found in many biological materials. Such material is readily extensible under low-strain deformation but becomes more resistant to extension at high-strain deformations, thus creating a "J" shaped stress-strain curve. Studying and mimicking such behavior would lead to bioinspired materials with self-protection mechanisms that can minimize premature failure from accidents or improper use. Existing strategies have primarily focused on introducing a hidden length in the material, either at the molecular or the bulk scale. Here, I demonstrate a new methodology that harnesses the squeeze behavior of magnetorheological fluid (MRF) to achieve the "J-shape" behavior. I encapsulated the MRF inside a soft polymer matrix, and the liquid-solid composites show adaptive "J-shape" mechanical responses. My study further demonstrates that the slope "J-shape" curve can be tuned by segmenting and manually activating specific MRF pockets. The "onset" of the "J-shape" curve could be programmed through integration with 3D wavy structures. This method enriched the library of fabricating bio-inspired materials and could potentially lead to self-protective, active materials for future wearable electronics or armor.

3.2 Introduction

Many soft biomaterials, though very thin and flexible, toughened themselves with a "J-shape" strain-stress behavior.[1,2] This mechanical behavior is characterized by a small stress increase under low-strain deformation in the initial stage, while it starts to have a dramatic stress growth under further large-strain deformation till failure. This type of adaptive behavior has also been known as the "strain-limiting" effect.[3] The exponentially increased resistance has been considered a key role in protecting materials from large deformation damage. Typical examples have been widely observed in nature, such as human skin,[4] human cardiac tissues,[5] spider silk,[6] etc. Those materials contain numerous curved and entangled collagen fibers. Once the tension strain is applied, it first de-curls or detangles the fibers, causing a negligible increase in stress. The stress quickly increases after the collagen has been straightened, and further elongation breaks the polymer chains.[3]

Replicating the "J-shape" behaviors in synthetic materials would lead to a self-strengthening and self-toughening adaptive material. The obtained materials would be very soft and flexible under low strains and gradually become stiffer in response to environmental changes when the strain becomes "dangerous" for the materials. Those characteristics are desirable for applications in next-generation electronics or armor, where the material can match the "J-shape" behaviors of human skin. Therefore, different approaches have been reported to mimic such "J-shape" behaviors.

Though many research papers have been published, recent approaches could be summarized and categorized into two types: 1) 2D patterning and 2) 3D structural engineering.[7] 1) 2D patterning usually embeds a flat 2D thin film in a pattern of wavy, horseshoe, or triangular shapes onto or into a flexible matrix.[3] Upon stretching, the curled pattern resembles the process of curled collagens being straightened up and generating a similar adaptive resistance. For example, Zhalmuratova et al.[8] sandwiched fabrics between silicone elastomer layers to get a fabric-reinforced elastomer composite. Their material offers strain-stiffening and anisotropic mechanical properties that closely replicate the "strain-stiffening" of the human aorta. Zhang et al.[9] used a similar sandwich structure to embed aramid fibers with a curvy pattern inside a polyurethane matrix to

mimic the gular sac tissue of the brown pelicans. Materials exclusively based on textiles[10] could also be viewed as another type of 2D patterning. A study showed that the external force must first uncoil the looped and interconnected knit, which requires the force to be relatively low in the beginning. The force needs to be dramatically increased at a later stage when it has to straighten the yarns, resulting in a process similar to that of many biomaterial cases.[10] 2) 3D structural engineering could be seen as an advancement of 2D patterning. The increased dimension gives the whole structure more freedom to preserve the hidden length or volume of the materials. Typical methods consist of employing designs like origami[11] or kirigami[12] to fold extra volume and release it during the stiffening stage. Other 3D structures, like helical[13,14] or octet[15,16], also have an additional length within their structures; therefore, materials experienced a "releasing" period before becoming stiffened. Those approaches mentioned above have advanced the field significantly; however, all of these strategies are heavily based on the same principal mechanism: add an additional step to release pre-stored excess length or volume, whether at the nano or macro scale, before the material gets stretched or compressed.

Here, I conceived a new strategy to replicate the "J-shape" behaviors that this work focuses on the material composition side (Figure 3.2 (a)). I prepared MRF composites and harnessed the squeeze behaviors to reproduce the "J-shape" mechanical behaviors of biomaterials. The liquid state material would endow the material with flexibility, allowing it to act like soft tissue; however, when compressed closer to the magnetic field, the MRF generates significant resistance, causing the material to stiffen and enhance the toughness of the composite. Compared with the previously mentioned methods, my method not only inherits the "J-shape" behaviors but also comes with more adaptability. This material generates a strong force even under larger deformation, and this force persists even after the material has leaked or failed. These findings will enrich the library of fabricating new wearable electronics and may lead to the creation of future armors.

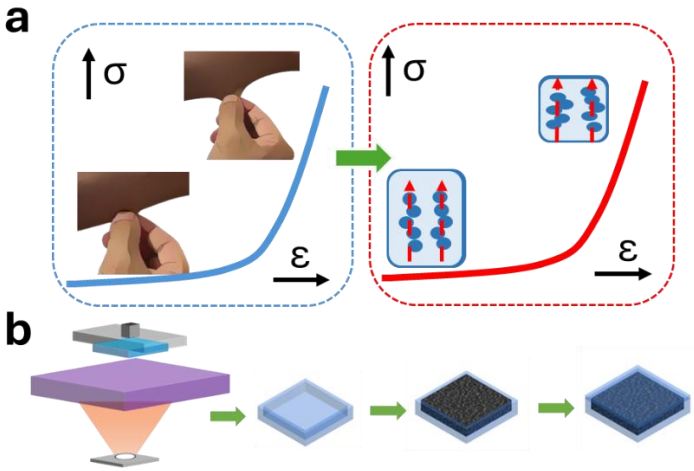

Figure 3.2 (a) Schematic of the proposed "J-shape" MR system. (b) Preparation process of the MRF pocket.

3.3 Material preparation and characterization

3.3.1 MRF preparation

The magnetorheological fluid was prepared by mixing 80 wt.% carbonyl iron particles (BASF CIP SQ, BASF SE, Germany) with 20 wt.% silicone oil (AR 20, Sigma-Aldrich) in mixer "Thinky" for 8 mins. Before mixing, carbonyl iron was coated with guar gum to avoid sedimentation and separation. The coating procedure was followed as described in the literature.[17,18]

Basically, 0.4 g guar gum (Fisher Science Education™ Guar Gum, Fisher Scientific) was dissolved in 70 mL deionized water, followed by adding carbonyl iron particles to the guar gum solution. After mixing at 850 rpm for 30 minutes, the coated particles were precipitated out by dropwise addition of ethanol. The obtained particles were washed with acetone and dried at 60℃ in a vacuum oven for 5 hours.

3.3.2 DLP printing of the matrix and encapsulation

I adopted my previous composition of DLP resin, a mixture of Ebecryl 8413 (Allnex) and Ebecryl 113 (Allnex) in a 1:0.2 weight ratio. The soft matrix was designed using Autodesk Inventor. A 3D printer, Masked Stereolithography Apparatus (Peopoly Phenom Forge), was used for all printing. The exposure time of each layer was set to 12.00 seconds. The exposure time of Superflex resin was adjusted to 3.00 seconds due to its faster curing speed. All printed samples were washed in isopropanol for 5 minutes and post-cured under UV light for 3 minutes. A stiffer matrix was DLP-printed by using commercial resin SuperFlex (3D Materials) with an exposure time of 3.0 seconds.

As shown in Figure 3.2 (b), the previously prepared MRF was injected into the DLP printed matrix. Then, the structure with the filled MRF was encapsulated by casting a resin layer, which was later cured with additional UV light for 3 minutes.

3.3.3 Characterization

3.3.3.1 Rheology tests

All rheology tests were performed on an Anton Paar MCR 102 rheometer at room temperature. For static normal force measurements of pure MRF, a certain amount of MRF was injected and placed on the plate. The gap between the upper and lower plates was set to 1 mm. Different magnetic fields have been turned on and off with a 30 sec/ 20 sec cycle repeated five times. The magneto-sweep test was performed with the same setup, but the magnetic field was varied within the window of [-0.8 T, +0.8 T]. The compression test of the MRF was conducted on the same setup, but with a moving upper plate compressing the MRF from 1 mm towards zero gap at a speed of 0.003 m/s.

3.3.3.2 Scanning Electron Microscopy (SEM)

The morphology of pristine and coated iron particles was observed using a Scanning Electron Microscope (Zeiss Gemini 500, ZEISS Company, Germany). Particles were dispersed in ethanol solution and then cast onto a wafer piece. After drying, samples were observed under an accelerating voltage of 3 kV.

3.3.3.3 Mechanical tests

Mechanical tests of the MRF pocket were performed on an Instron 3369 universal machine. For the static normal force measurements, the magnetic field was generated by the electromagnet (12 V, 25 N, Uxcell) underneath the sample (see the Setup image in Figure 3.3.3.3.1). A DC power supply (Dr. Meter PS-305DM) was connected to the electromagnet to tune the magnetic field.

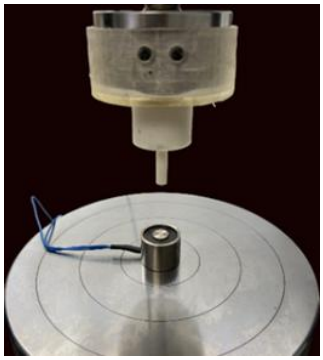

Figure 3.3.3.3.1 Setup image of static normal force measurements.

Dynamic compression of the MRF pocket was also performed on an Instron. The magnetic field source was supplied by ceramic magnets with an average magnetic field of 0.15 T. A customized stiff plastic plate had been installed on the upper plate to avoid the steel plate being attracted by the magnets. The pattern test used a similar setup, but with a plastic bed plate (see Figure 3.3.3.3.2). The plastic bed plate has a 3×3 cavity array that matches the MRF pocket size. The cavity could be filled with either a plastic rod or a magnet; the former has no magnetic field, while the latter provides one.

Figure 3.3.3.3.2 Setup image of compression test for MRF pocket array.

3.4 Analysis and discussion

3.4.1 In searching for a strong resistance force of MRF

MRF contains metal particles dispersed in liquid carriers; therefore, there's a mismatch in density between pure iron particles and silicone oil. This mismatch causes sedimentation and separation in the system. Based on the literature,[17,18] I chose the guar gum coating for its simplicity and effectiveness in addressing the density mismatch. Successful coating was confirmed by SEM images (Figure 3.4.1.2), where the coated particles have a size of 2.23 ± 1.11 μm, compared to the pristine CI particles of 1.69 ± 1.11 μm.

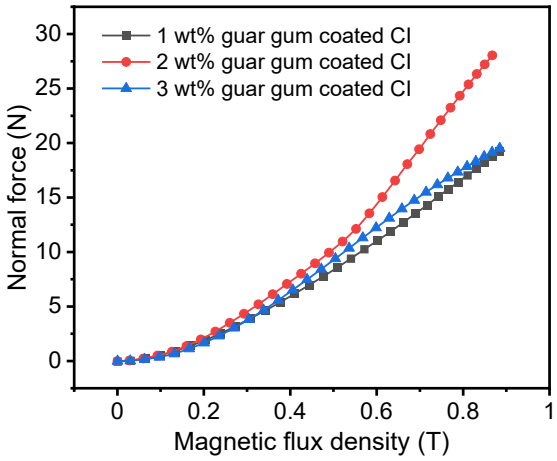

Figure 3.4.1.1 Normal force of MRF with different guar gum coating additions.

The rheology results show that the addition of 2 wt.% guar gum yields the highest normal force (Figure 3.4.1.1); therefore, a 2 wt.% guar gum coating was used for all my experiments. Coated polymer may act as a stress "buffer", reducing interactions between iron particles, thereby causing the decrease in normal force (Figure 3.4.1.3. (c)). On the other side, it's also essential to consider its improved stability, as only 2~3% of the MRF sedimented after 3 months. A well-dispersed MRF with high stability is necessary to ensure durability and cyclability.

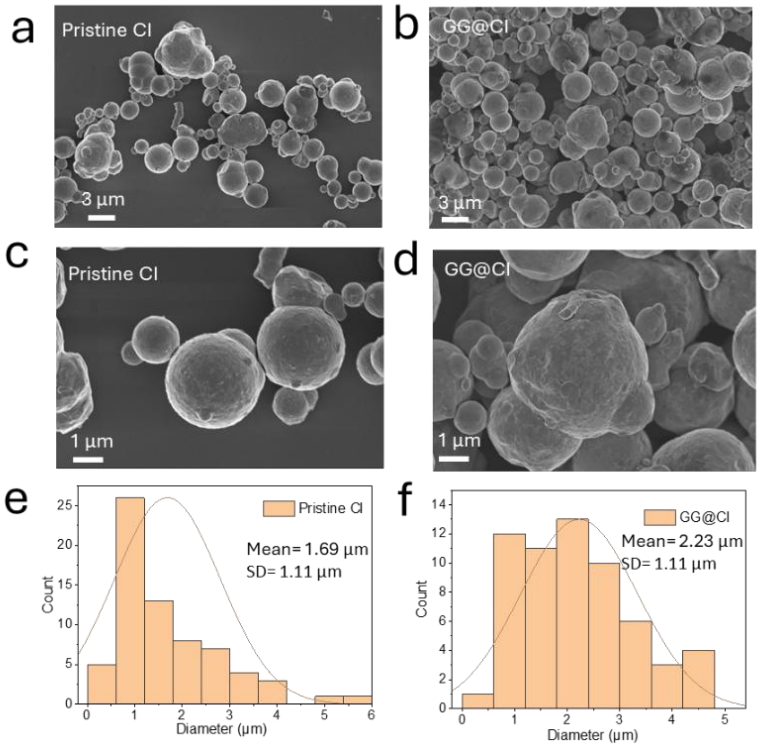

Figure 3.4.1.2 SEM images and particle size distributions of pristine and treated CI particles. (a), (c) and (e) are pristine CI; (b), (d), and(f) are guar gum-coated CI.

To test whether MRF could generate a desirable resistance force, I first tested the normal force of MRF under static conditions. In this test, the gap between the upper and lower plates of the rheometer was maintained at a constant value. The gauge sensor on the upper plate recorded the normal force generated by the magnetic clusters of the MRF. Three magnetic fields, 0.2, 0.7, and 0.9 T, were applied separately, representing low, medium, and high fields, respectively. Results are shown in Figure 3.4.1.3. (a) and (b), which show that the MRF responded simultaneously to the magnetic fields when the fields were "on" and "off". MRF is a field-responsive matter; it has a low response time, and each switch between "on/off" in this test is less than 0.1 sec. I believe my measuring instrument limits this value; the actual responding time could even be lower, which would enable the MRF to adapt to the field within a shorter time. With that fast-responding speed, normal force immediately increased from 0.0 N to 1.7 N, 0.0 N to 15.0 N, and 0.0 N to 26.0 N (Figure 3.4.1.3 (a)). While the magnetic field ranged from 0.2 T to 0.9 T, representing a 4.5-fold increase, the normal force experienced a more than 15-fold increase. Studies ascribed the normal force to the repulsive force of magnetic clusters of MRF.[19] When exposed to a magnetic field, particles interact with each other, forming chain-like or column-like structures. Those newly formed magnetic clusters offered support to the liquid; therefore, the gauge sensor was able to record the normal force.

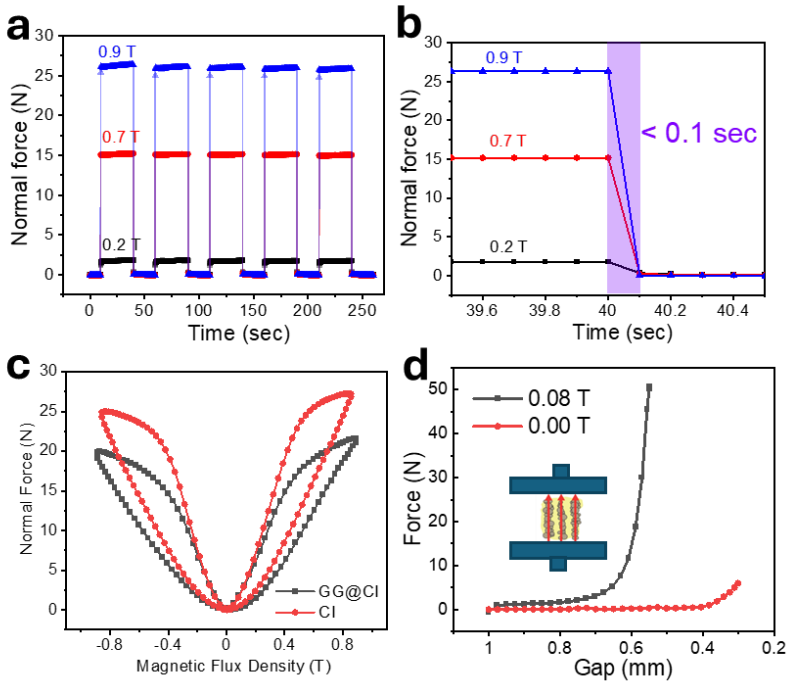

Figure 3.4.1.3 (a) and (b) Normal force of MRF with magnetic fields "ON" and "OFF". (c) Normal force of MRF with a varying magnetic field. (d) The squeezing behavior of MRF.

In addition to the discrete values of the magnetic field, I then applied a continuous magnetic field that gradually increased or decreased within the range of [-0.8 T, +0.8 T]. The MRF demonstrated excellent tunability, as shown in Figure 3.4.1.3(c). The normal force went continuously back and forth within a 0-25 N range, showing its adaptability in response to external field changes.

However, fluid without any stretch or compression is an overly idealized condition. It's important to test how MRF responds to dynamic deformation. Here, I also did a compression test on MRF using the rheometer (Figure 3.4.1.3 (d)). In this test, the upper plate moved downwards to compress the MRF on a fixed lower plate with a weak magnetic field 0.08 T. Compared with the control group (which has a slight increase in the end because of the densification), the MRF with magnetic field "on" exhibits an exponentially increased force in a "J" shape that quickly reaches to the limit of the gauge sensor of the instrument. This dramatic mechanical response could be attributed to the squeezing behaviors of MRF. Researchers had attributed this significant increase to being predominantly caused by a closer distance to the magnetic field, where the resistance force is directly proportional to the magnetic field.[20] It has also been pointed out that compression also reformed chain structures of iron particles, leading to an increasing number of shorter and thicker robust columns/body-centered cubic (BCC) structures.[20,21] To protect the equipment from overload, I used a weak field of 0.08 T for demonstration. But the MRF already showed a 50 N increase even under this weak field. This result indicates that the squeezing behaviors of MRF not only demonstrate its potential as a tunable and adaptive material for replicating "J-shape" behaviors but also highlight its ability to reduce reliance on strong magnetic fields, which are unsafe for practical applications.

3.4.2 Transferred the resistance from pure liquid to composites?

Pure MRF itself shows promising "J-shape" behaviors; however, it's important to encapsulate the liquid-state MRF inside a matrix so that it could be easily handled or integrated into devices.[22–25] The key question is whether the strong resistance of pure fluid could be transferred to the liquid-solid composites after encapsulation. To explore this, I DLP-printed a cubic mold with a cavity inside. The printed soft matrix has a low modulus and good stretchability, which avoids interference with the resistance generated by the fluid. It will also help to maintain the integrity of the composites under large strains.

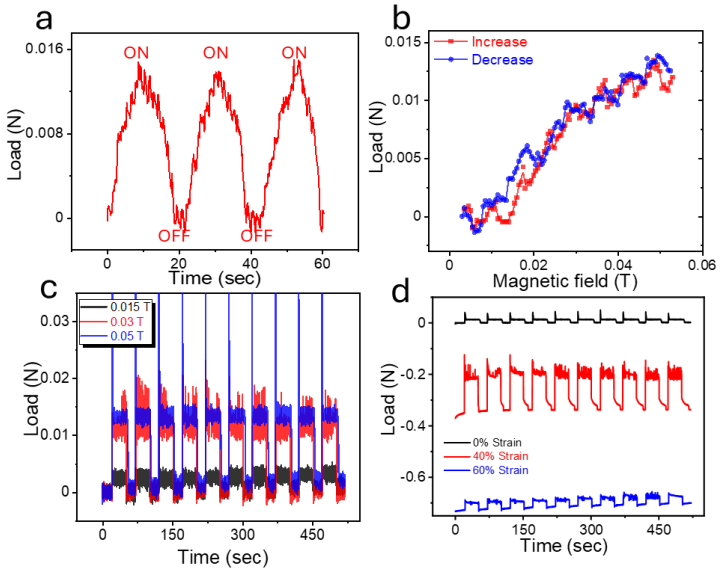

Figure 3.4.2.1 (a) and (b) Normal force of MRF pocket with tuning magnetic field within 0 T to 0.05 T. (c) Normal force of MRF pocket with different magnetic field values "ON" and "OFF". (d) Normal force of MRF pocket at different strains with magnetic field "ON" and "OFF".

I first examined the static normal force of the MRF composite. A small MRF pocket with a 10 mm ×10 mm × 4.5 mm dimension was prepared and placed on an electromagnet with a

customized plastic tip contacting its surface. The sample exhibited normal force "on/off" switching behaviors and demonstrated good tunability, similar to pure MRF (Figure 3.4.2.1 (a)-(d)). With that success, I started testing the resistance under dynamic compression. As we can see from Figure 3.4.2.2 (a), the MRF composites exhibit the "J-shape" stress-strain behaviors even without the magnetic field. This is because of the intrinsic characteristics that MRF is a liquid-state matter, and thus is incompressible. The hydrostatic pressure offers resistance during the compression, as reported in research.[26] Compared with the non-magnetic field case, samples compressed with an average of 0.15 T show a steeper "J" curve (Figure 3.4.2.2 (a)). Samples experienced an exponentially stiffened process and became stiffer than non-magnetic field samples after 20% strain. This result confirms that the MRF composites could actively maintain the same level of "J-shape" behavior as pure MRF, though the stiffening rate slows down to some extent due to the polymer encapsulation.

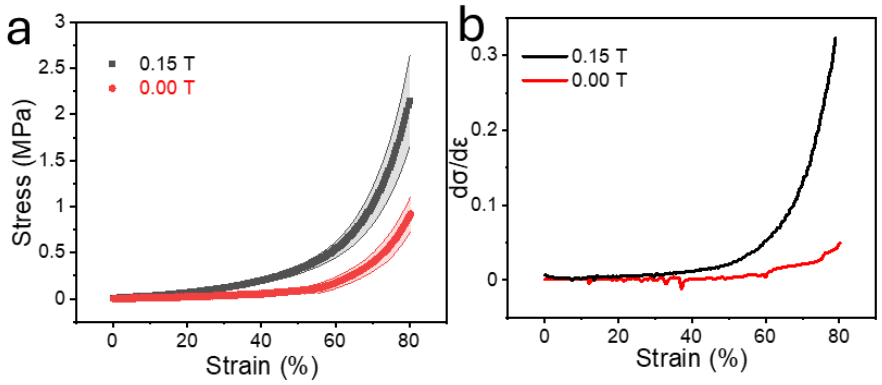

Figure 3.4.2.2 (a) Strain-stress behaviors of MRF pocket under compression. (b) Differential of strain-stress curve under compression.

Interestingly, I observed that after the composites failed and the MRF leaked out, the MRF continued to function. The magnetic field attracted the particles, thereby confining their movement at all times. To better study this, I took the derivative of the stress-strain curve of the most representative sample curve (Figure 3.4.2.2(b)). The small fluctuations and peaks indicate the release of stress, suggesting that possible leaks of MRF occurred in this sample. From the curve, we can see that the sample tested with no magnetic field is quite vulnerable. The curve exhibits small peaks throughout, indicating that leakage may occur throughout the entire process. In contrast, the sample compressed with the magnetic field has far fewer peaks. Most of the leaked MRF gathered around the leakage holes. This is significant because it suggests that the active matter can function as an adaptive component even after being damaged, persisting until the composites reach failure.

3.4.3 Geometry factors of J-shape behaviors

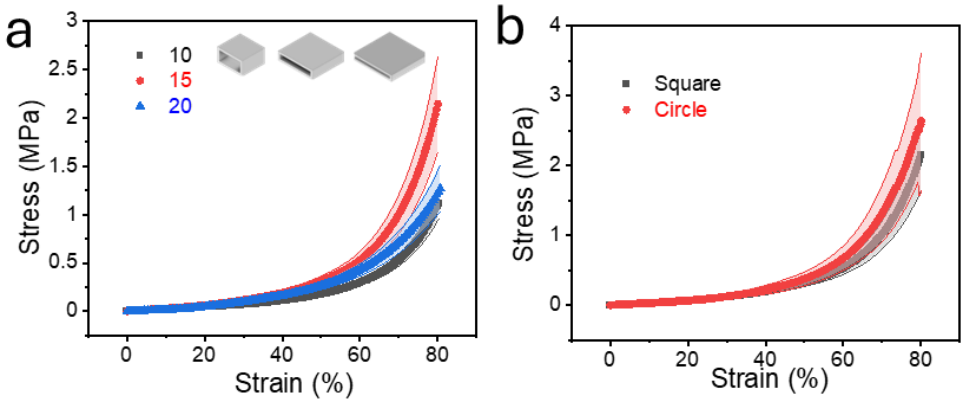

Figure 3.4.3.1 (a) Strain-stress curves of MRF pockets with different "brick" sizes. (b) Strain-stress curves of MRF pockets with different shapes.

The next question I wonder is whether the "J-shape" behaviors could be controlled by geometry tuning. I specifically chose the distance of the height center to the magnets and the shape of the MRF pocket as my focus since the former one determines, on average, how close the fluidic pocket is to the magnetic field, while the latter may shape the way the liquid pocket expands upon compression. Firstly, I kept the MRF pocket volume constant but changed the thickness of the pocket to adjust the height, thus getting samples with dimensions of 20 mm × 20 mm × 1.125 mm, 15 mm × 15 mm × 2 mm, and 10 mm × 10 mm × 4.5 mm (Figure 3.4.3.1 (a)). The three types of samples do not show a significant difference in stress-strain curves, while the 15 mm × 15 mm sample has a slightly stronger resistance force than the other two under larger deformations. As for the geometry shape experiment, the results for cubic and cylindrical samples are even more identical (Figure 3.4.3.1(b)). These two curves almost overlapped. Mechanical tests from the above two experiments suggest that the height center and sample shape may play a role in determining the "J-shape" behaviors, but their influence is minimal. The volume of MRF in each pocket may play a more significant role in determining the "J" curves, as more magnetic particles are involved in these systems (Figure 3.4.3.2).

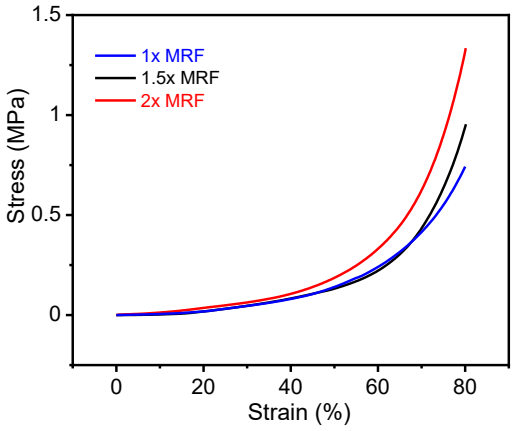

Figure 3.4.3.2 Stress-strain curves of MRF pockets with different MRF volume loading (1x, 1.5x, and 2x).

3.4.4 Manipulation of stiffness and localized pattern

Although the structural parameters of the pocket did not appear to significantly influence the "J-shape" curve, I found that the segmentation of the MRF pocket led to a few interesting behaviors.

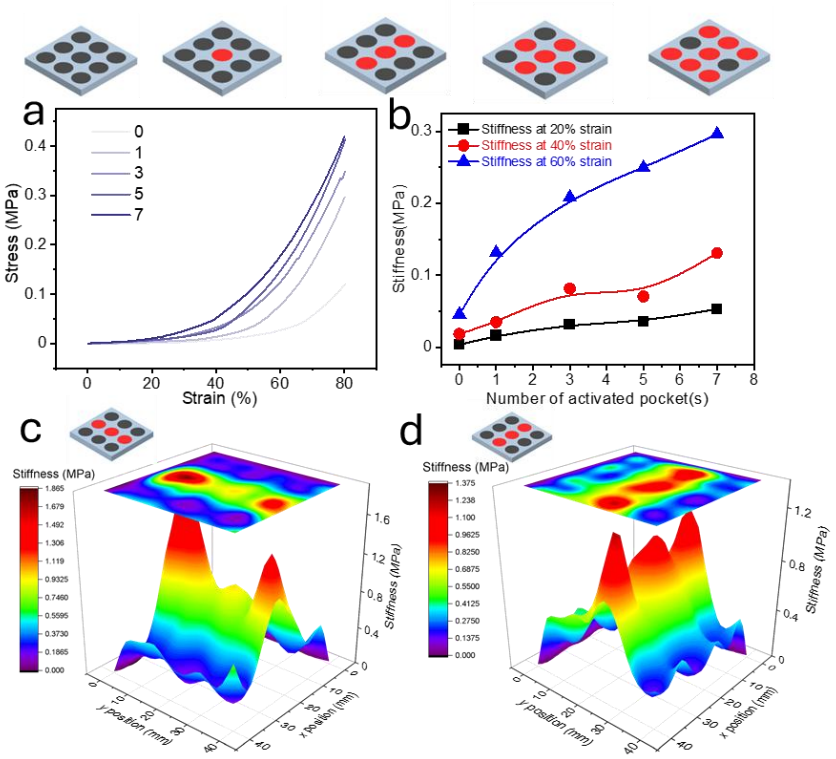

Figure 3.4.4.1 (a) Strain-stress curves of MRF pocket array with the activation number of 0, 1, 3, 5, and 7. (b) Stiffness of the MRF array at different compression strains with varying activation number. (c) Stress mapping of horizontally activated three pockets. (d) Stress mapping of vertically activated three pockets.

Segmentation of liquid pockets has been an effective method to avoid the catastrophic leakage of active liquid content. Therefore, I created a 40 mm × 40 mm × 4 mm sample with MRF pockets arranged in a 3 × 3 array. A magnet of the same size underneath can control the activation of each small MRF pocket. Therefore, I tested the sample with 0, 1, 3, 5, and 7 pockets activated each time. Figure 3.4.4.1 (a) shows that with more pockets activated, composites got further stiffened, thus leading to a steeper "J" curve. By extracting data from Figure 3.4.4.1 (a), I replot the graph to compare the degree of stiffening effect at different deformations. In obtained graph Figure 3.4.4.1 (b), in response to the activated number increase from 0 to 7, the stiffness of 20% strain increased from 0.003 MPa to 0.05 MPa, the slope of the curve hits 0.007 MPa, while the slope of the 40% strain increased to 0.016; in stark contrast, the slope kept increasing to 0.036 under the 60% strain. The reason why larger deformation stiffened the material more could be explained by the characteristics of the "soft-hard" transition behaviors of MRF. Under low compression strains, iron particles are in weak chains; therefore, the mixture behaves more like a fluid. In this case, an increased number of activated pockets will not have a significant influence on the "J" curve or stiffness. However, as it was being compressed closer to the magnet, the MRF started acting more like a "paste". The contribution of resistance from each individual pocket is no longer negligible; thus, the activation number has a dramatic influence on stiffness. The slope change of the "J-shape" curves implies that we can effectively tune the "J-shape" behaviors by segmenting and separately

activating the pockets. This feature makes the MRF composite a stiffness-manipulable material system.

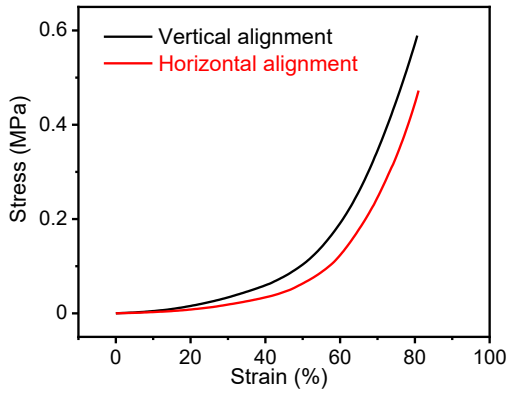

Figure 3.4.4.2 Stress-strain curves of three activated MRF pockets aligned in different patterns.

The segmentation of the MRF pocket not only provides an opportunity to tune the mechanical properties, but it also enables active manipulation and localization to be possible. Here, I did a demonstration to show the flexibility of activating different patterns within those pockets. In Figure 3.4.4.1 (c) and (d), I used magnets arranged in two different patterns to activate the pocket array. These three magnets are aligned (1) in a horizontal line and (2) in a vertical line. The two samples exhibit almost identical compression "J" curves, as shown in Figure 3.4.4.2. However, we can clearly observe the orientation difference in the stress mapping images. In my demonstration, I used only a 3×3 pocket array for illustration; however, a larger plane with more MRF pocket arrays could be achieved. Each pocket will act like a "pixel" for a higher degree of accurate manipulation and patterning of the material's stiffness. Similar patterning methods have been reported.[27] However, those methods usually relied on the pretreatment of the sample with a fixed pattern. In my system, the pattern could be changed freely, easily, and swiftly based on the needs of real applications.

3.4.5 Integrated MRF with 3D structures

So far, all of my previously mentioned samples are confined to a thin 2D pocket, which has limited structural complexity. I started wondering what a 3D structure would bring to this system if I encapsulated the MRF within a 3D-printed structure.

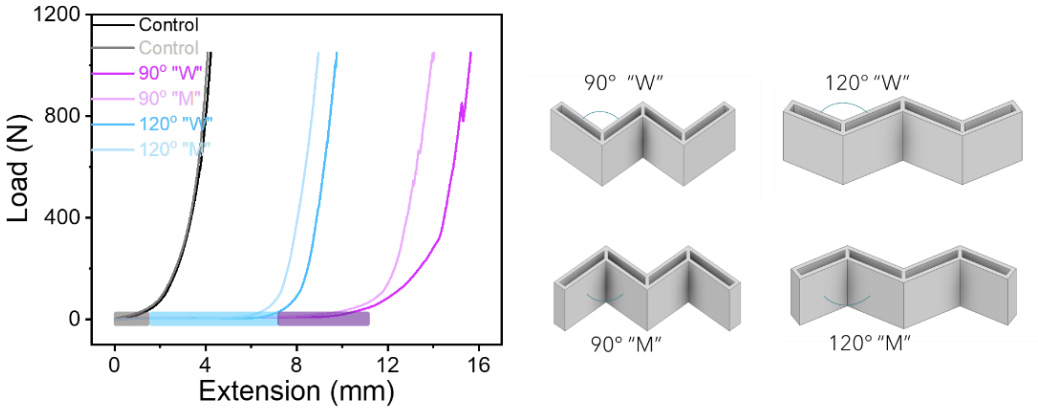

Figure 3.4.5.1 Load-extension curves of MRF in wavy structures. Control groups are 2D sheet pockets compressed from the top and the bottom sides.

To explore this, I chose the wavy structure as the starting point, as it has been reported to generate a "J-shape" response; therefore, it will not offset the "J" behavior of MRF. I DLP-printed a wavy structure that could be viewed as four independent sheet pockets connected (Figure 3.4.5.1). The previous resin is too soft to support the structure. Hence, I adopted a stiffer commercial resin, SuperFlex, as the matrix material. The intersection angle between each sheet pocket could be varied; I adopted 120° and 90° as representative angles, which would help explore the general trend of mechanical behaviors from a totally flat pocket to more folded structures. The wavy structure has two orientations, "M" and "W". I investigated both orientations as well to see if they have an effect on the mechanical behaviors.

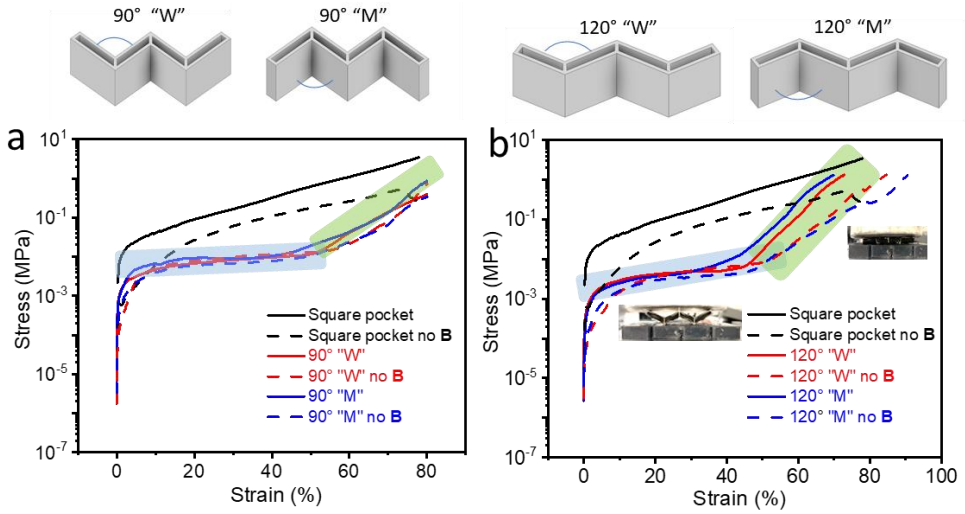

Figure 3.4.5.2 Strain-stress curves of MRF in wavy structures with the log scale. (a) intersection angle of 90°. (b) Intersection angle of 120°.

Figure 3.4.5.1 shows the compression results of those 3D samples. Compared to the control group, the 3D samples undergo an additional step in the compression process, where the wavy structures are compressed before the pocket. Due to this reason, the 3D samples exhibit a long "low strain" region, where the resistance starts to increase dramatically from 60% strain. This indicates that embedding the MRF in a wavy structure would enable the "onset" transition of the "J-shape" to be programmed. By decreasing the intersection angle, the stiffening stage could be postponed. I also noticed that wavy samples with "M" or "W" orientation behave similarly. The only difference is that the "onset" of the "M" orientation is always ~1% strain earlier than that of "W". This is probably because the "M" shape has more contacts (3 points vs. 2 points) with the magnets underneath, therefore it was subjected to a stronger attraction force, which limits its ability to be deformed and flattened.

Interestingly, after I switched the y-axis to a log scale, I found that the increased complexity in structure also brings multiple levels of responses to the composites. As shown in Figure 3.4.5.2, the first stage of wavy structure compression results in a low increasing rate, where the material remains insensitive to the compression force. The latter stage is primarily the compression of MRF, resulting in a significantly faster increasing rate, which means the material has become exponentially stiffer. This differentiates the 3D structure from the 2D sheet pocket, which only has a constant increasing rate.

In addition to the wavy structure, I also explored MRF in a printed "X" shape structure. This structure shows a sequential folding sequence under compression. During the stages from "0" to "2", the upper two layers were mainly compressed. Then, from "2" to "3", the lower two layers were compressed until they were attracted to the surface by the magnets. From "4" to "5", both upper and lower layers were compressed, but the upper layer deformed more than the lower. From "5" to the end, both upper and lower layers were compressed equally. This multiple-step folding leads to multiple-level responses to the external force (Figure 3.4.5.3 (a)-(c)). The curve also shows an interesting "click" point (Point 3) where the material suddenly got attracted by the magnets. This "click" point may serve as a "gate" strain value, allowing us to program and set it to activate the "J-shape" protection of the material. However, this structure did not show much MRF-induced stiffening effect until a very large strain (Figure 3.4.5.3 (c), blue point). The upper two pockets may act as a stress "buffer" for the lower two layers, thus dissipating some energy. The stiffening started to take effect when both the upper and lower layers were compressed close enough to the magnets. As a result, the "Onset" strain of stiffening was delayed to the very large strain. This might tell us that multiple layers of "X" shape bring a more complicated behavior pattern to the material system, which allows us to further program the adaptive behaviors of the material system. However, it comes with a cost of further delay of the "Onset" stiffening strain.

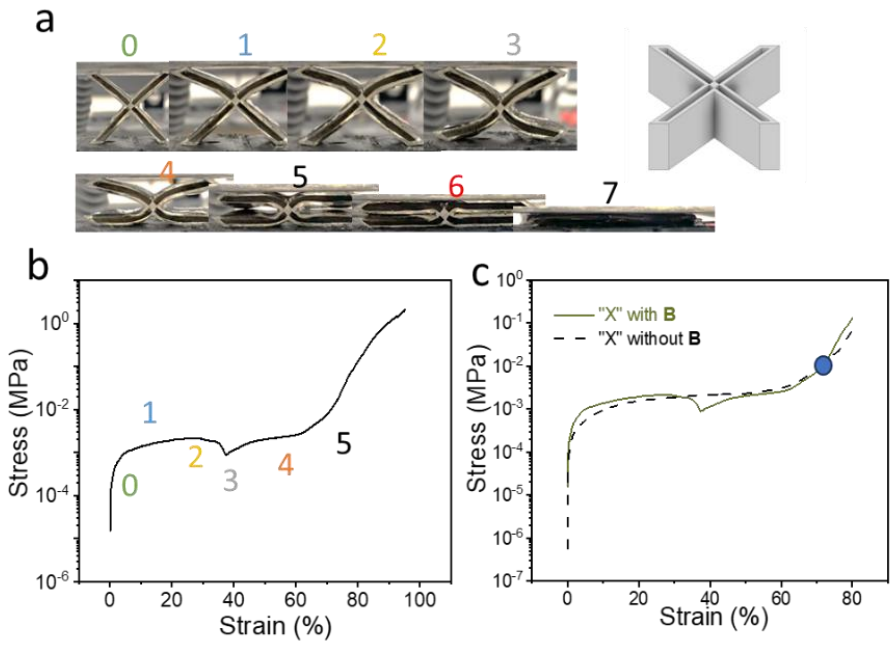

Figure 3.4.5.3 Compression of MRF in "X" shape beams. (a) Images of "X" shape beams being compressed. (b) and (c) Strain-stress curves of the compression.

3.5 Conclusion

In this work, I propose using the squeezing behaviors of MRF to prepare a material that mimics the "J-shape" stress-strain behaviors. Under compression, this material exhibits low resistance to mechanical deformation under low compression strains, while it starts generating dramatically greater resistance when compressed to large strains. I found that the geometry of the MRF pocket does not have a strong influence on the "J-shape" curve. However, the segmentation and specific activation of the MRF pocket array make it possible to tune the slope of the "J" curve. This allows us to adjust the sensitivity of the composite getting stiffened. Integrating the MRF

pockets with 3D wavy structures endows the material with a few new characteristics: (1) it gives us the option to program the "onset" strain of "J-shape" curves by specifically designing the intersection angle of each pocket (2) it leads to a dual-level of response of material to the external force. Materials with those characteristics may find potential applications in future electronic materials and armor systems.

3.6 References

(1) Yang, W.; Sherman, V. R.; Gludovatz, B.; Schaible, E.; Stewart, P.; Ritchie, R. O.; Meyers, M. A. On the Tear Resistance of Skin. *Nat. Commun.* **2015**, *6* (1), 6649. https://doi.org/10.1038/ncomms7649.

(2) Chamiot-Clerc, P.; Copie, X.; Renaud, J.-F.; Safar, M.; Girerd, X. Comparative Reactivity and Mechanical Properties of Human Isolated Internal Mammary and Radial Arteries. *Cardiovasc. Res.* **1998**, *37* (3), 811–819. https://doi.org/10.1016/S0008-6363(97)00267-8.

(3) Ma, Y.; Feng, X.; Rogers, J. A.; Huang, Y.; Zhang, Y. Design and Application of 'J-Shaped' Stress–Strain Behavior in Stretchable Electronics: A Review. *Lab. Chip* **2017**, *17* (10), 1689–1704. https://doi.org/10.1039/C7LC00289K.

(4) Nicolle, S.; Decorps, J.; Fromy, B.; Palierne, J.-F. New Regime in the Mechanical Behavior of Skin: Strain-Softening Occurring before Strain-Hardening. *J. Mech. Behav. Biomed. Mater.* **2017**, *69*, 98–106. https://doi.org/10.1016/j.jmbbm.2016.12.021.

(5) Rahman, F.; McEvoy, J. W. The J-Shaped Curve for Blood Pressure and Cardiovascular Disease Risk: Historical Context and Recent Updates. *Curr. Atheroscler. Rep.* **2017**, *19* (8), 34. https://doi.org/10.1007/s11883-017-0670-1.

(6) Meyers, M. A.; McKittrick, J.; Chen, P.-Y. Structural Biological Materials: Critical Mechanics-Materials Connections. *Science* **2013**, *339* (6121), 773–779. https://doi.org/10.1126/science.1220854.

(7) Hanif, A.; Yoo, D.; Kim, D.; Mustafayev, F.; Hajiyev, S.; Kim, D. S. Recent Progress in Strain-Engineered Stretchable Constructs. *Int. J. Precis. Eng. Manuf.-Green Technol.* **2024**, *11* (4), 1403–1433. https://doi.org/10.1007/s40684-023-00565-w.

(8) Zhalmuratova, D.; La, T.-G.; Yu, K. T.-T.; Szojka, A. R. A.; Andrews, S. H. J.; Adesida, A. B.; Kim, C.; Nobes, D. S.; Freed, D. H.; Chung, H.-J. Mimicking "J-Shaped" and Anisotropic Stress–Strain Behavior of Human and Porcine Aorta by Fabric-Reinforced Elastomer Composites. *ACS Appl. Mater. Interfaces* **2019**, *11* (36), 33323–33335. https://doi.org/10.1021/acsami.9b10524.

(9) Zhang, H.; Shu, J.; Liu, Z.; Wu, J. High-Performance Crack-Resistant Elastomer with Tunable "J-Shaped" Stress–Strain Behavior Inspired by the Brown Pelican. *ACS Appl. Mater. Interfaces* **2022**, *14* (19), 22489–22496. https://doi.org/10.1021/acsami.2c06646.

(10) Maziz, A.; Concas, A.; Khaldi, A.; Stålhand, J.; Persson, N.-K.; Jager, E. W. H. Knitting and Weaving Artificial Muscles. *Sci. Adv.* **2017**, *3* (1), e1600327. https://doi.org/10.1126/sciadv.1600327.

(11) Filipov, E. T.; Paulino, G. H.; Tachi, T. Origami Tubes with Reconfigurable Polygonal Cross-Sections. *Proc. R. Soc. Math. Phys. Eng. Sci.* **2016**, *472* (2185), 20150607. https://doi.org/10.1098/rspa.2015.0607.

(12) Isobe, M.; Okumura, K. Initial Rigid Response and Softening Transition of Highly Stretchable Kirigami Sheet Materials. *Sci. Rep.* **2016**, *6* (1), 24758. https://doi.org/10.1038/srep24758.
(13) Jia, B.; Yu, L.; Fu, F.; Li, L.; Zhou, J.; Zhang, L. Preparation of Helical Fibers from Cellulose–Cuprammonium Solution Based on Liquid Rope Coiling. *RSC Adv.* **2014**, *4* (18), 9112. https://doi.org/10.1039/c3ra47031h.
(14) Pham, J. T.; Lawrence, J.; Lee, D. Y.; Grason, G. M.; Emrick, T.; Crosby, A. J. Highly Stretchable Nanoparticle Helices Through Geometric Asymmetry and Surface Forces. *Adv. Mater.* **2013**, *25* (46), 6703–6708. https://doi.org/10.1002/adma.201302817.
(15) Yan, D.; Chang, J.; Zhang, H.; Liu, J.; Song, H.; Xue, Z.; Zhang, F.; Zhang, Y. Soft Three-Dimensional Network Materials with Rational Bio-Mimetic Designs. *Nat. Commun.* **2020**, *11* (1), 1180. https://doi.org/10.1038/s41467-020-14996-5.
(16) Jordan, R. S. 3D Printed Architected Conducting Polymer Hydrogels. *J Mater Chem B* **2021**, 13. https://doi.org/10.1039/D1TB00877C.
(17) Fang, C.; Zhao, B. Y.; Chen, L. S.; Wu, Q.; Liu, N.; Hu, K. A. The Effect of the Green Additive Guar Gum on the Properties of Magnetorheological Fluid. *Smart Mater. Struct.* **2005**, *14* (1), 1–5. https://doi.org/10.1088/0964-1726/14/1/N01.
(18) Wu, W. P.; Zhao, B. Y.; Wu, Q.; Chen, L. S.; Hu, K. A. The Strengthening Effect of Guar Gum on the Yield Stress of Magnetorheological Fluid. *Smart Mater. Struct.* **2006**, *15* (4), 94–98. https://doi.org/10.1088/0964-1726/15/4/N04.
(19) Yao, X.-Y.; Yu, M.; Fu, J. Magnetic-Enhanced Normal Force of Magnetorheological Fluids. *Smart Mater. Struct.* **2015**, *24* (3), 035001. https://doi.org/10.1088/0964-1726/24/3/035001.
(20) Guo, C.; Gong, X.; Xuan, S.; Yan, Q.; Ruan, X. Squeeze Behavior of Magnetorheological Fluids under Constant Volume and Uniform Magnetic Field. *Smart Mater. Struct.* **2013**, *22* (4), 045020. https://doi.org/10.1088/0964-1726/22/4/045020.
(21) Ismail, I.; Mazlan, S. A.; Zamzuri, H.; Olabi, A. G. Fluid–Particle Separation of Magnetorheological Fluid in Squeeze Mode. *Jpn. J. Appl. Phys.* **2012**, *51* (6R), 067301. https://doi.org/10.1143/JJAP.51.067301.
(22) Song, G.; Qian, Z.; Liu, X.; Chen, B.; Li, G.; Wang, Z.; Wang, K.; Zou, Z.; Galbusera, F.; Domingos, M.; Ren, L.; Wilke, H.; Ren, L. Bioinspired Intervertebral Disc with Multidirectional Stiffness Prepared via Multimaterial Additive Manufacturing. *Adv. Funct. Mater.* **2023**, *33* (44), 2300298. https://doi.org/10.1002/adfm.202300298.
(23) Testa, P.; Style, R. W.; Cui, J.; Donnelly, C.; Borisova, E.; Derlet, P. M.; Dufresne, E. R.; Heyderman, L. J. Magnetically Addressable Shape-Memory and Stiffening in a Composite Elastomer. *Adv. Mater.* **2019**, *31* (29), 1900561. https://doi.org/10.1002/adma.201900561.
(24) Hong, S.-W.; Yoon, J.-Y.; Kim, S.-H.; Lee, S.-K.; Kim, Y.-R.; Park, Y.-J.; Kim, G.-W.; Choi, S.-B. 3D-Printed Soft Structure of Polyurethane and Magnetorheological Fluid: A Proof-of-Concept Investigation of Its Stiffness Tunability. *Micromachines* **2019**, *10* (10), 655. https://doi.org/10.3390/mi10100655.
(25) Bastola, A. K.; Li, L.; Paudel, M. A Hybrid Magnetorheological Elastomer Developed by Encapsulation of Magnetorheological Fluid. *J. Mater. Sci.* **2018**, *53* (9), 7004–7016. https://doi.org/10.1007/s10853-018-2012-2.

(26) Zhang, X.; Wang, P.; Kurkin, A.; Chen, Q.; Gong, X.; Zhang, Z.; Yang, E.-H.; Yang, J. Mechanical Response of Shear Thickening Fluid Filled Composite Subjected to Different Strain Rates. *Int. J. Mech. Sci.* **2021**, *196*, 106304. https://doi.org/10.1016/j.ijmecsci.2021.106304.
(27) Yu, K.; Feng, Z.; Du, H.; Xin, A.; Lee, K. H.; Li, K.; Su, Y.; Wang, Q.; Fang, N. X.; Daraio, C. Photosynthesis-Assisted Remodeling of Three-Dimensional Printed Structures. *Proc. Natl. Acad. Sci.* **2021**, *118* (3), e2016524118. https://doi.org/10.1073/pnas.2016524118.

Chapter 4
Bio-inspired adaptive and transformable mold

4.1 Abstract

Digital Light Processing (DLP) printing attracts intensive attention as it provides fast fabrication and high structural complexity that are difficult to achieve through traditional fabrication methods. But the photochemical nature of its printing mechanism places demanding criteria on chemical reactivity, rheological, and photo-responsive properties of the resin, thus limiting the diversity of printable materials. The DLP-assisted mold injection method was identified a possible remedy. The DLP-printed complex structure is subsequently used to shape a meltable or thermally curable material. This method opens the door for a significantly wider array of materials to be 3D structured. However, current DLP-assisted mold injection methods lack the adaptability to change mold sizes. The mold in the same structure but with different sizes needs to be printed, leading to an increase in the manufacturing costs. To address this, I conceived the idea to mimic the "bulking" behaviors of pufferfish and prepared an adaptive and transformable mold that allows for dynamic infill size control. I explored the criteria for choosing the hydrogel material. I selected poly(2-acrylamido-2-methyl-1-propanesulfonic acid) (poly(AMPS)) as my base material because of its preferred size tunability and satisfactory mechanical integrity upon dehydration/hydration. I also studied how crosslinking ionic species and drying method influenced the thermal stability (ability to endure thermally curable material) and mechanical integrity (ability to support the infills). My prepared mold could be versatilely designed and printed, and was able to be manipulated to the intended volume for different infill injections.

4.2 Introduction

With the advent of 3D printing techniques, it has quickly gained popularity in material manufacturing as it overcomes the constraints imposed by traditional manufacturing methods.[1–3] Among those, DLP printing is one of the most promising techniques that achieves fast fabrication speed and high resolution because of its intrinsic advantages of photopolymerization kinetics.[4,5] However, the success of DLP printing is heavily reliant on the finely tuned photo-reactive resin. Solvents and monomers have been carefully selected and optimized to achieve the required rheological, chemical, and optical properties of the ink.[4] These requirements restrict the material diversity for DLP printing. As a result, it has been found to be challenging to embody a large amount of metal,[6] ceramic,[7] and conductive polymer[8–10] in prints. Those materials interfere with light scattering and absorption during the production.

To overcome these issues, alternative methods based on DLP have been reported.[11–13] One example, from Saccone et al.,[14] used DLP printed lattices as a scaffold to absorb metal-ion solutions. After dehydration, calcination, and reduction, they were able to get pure metals such as Cu, Ni, Ag, and other alloys in a complex structure. This work allows for the 3D structuring of metal without the direct 3D printing of metal, which usually requires expensive equipment and high energy input. Another example, by Hill et al.,[15] illustrated a method to create a complex 3D conducting polymer, which has been traditionally difficult to print by DLP. This method combines DLP printing and precursor injection. Monomers were cast into the DLP printed mold and were then converted to polymer in the solid state inside the mold. Through this method, a variety of conducting polymers could be processed into 3D structures with high complexity. Although more materials can now be manufactured through those methods, the choices of degradable molds are limited. Those molds usually cannot endure elevated temperatures, which makes them incompatible with many polymers, such as thermoplastics, that need to be processed via melting and casting. Furthermore, those

traditional molds are static, meaning the shape and size of their cavities are replicated by casting parts. A need to change the size would mean a new mold needs to be designed and printed, which requires additional labor and cost. A mold with tunable sizes post-printing could enable dimensional-tuning or alteration on the fly, minimizing the production turnaround time and hence enhancing printing efficiency.

In nature, through the long history of evolution and adaptation, pufferfish developed the survival skills to inflate themselves by swallowing a large amount of water or air to deter predators.[16] Inspired by that, I conceived the idea to create an adaptive and transformable hydrogel mold using the superabsorbent material. The superabsorbent polymer is readily able to expand several times larger with a quick absorption of a large amount of water. It could mimic the "bulking" behaviors of pufferfish and apply this principle to the design of DLP printed adaptive molds, which would enable modulation of the volume of infills. Specifically, in this paper, I investigated the prerequisites of choosing a suitable hydrogel base material. I also studied the crosslinking effects of different ion species and drying methods on the post-processing treatment of the hydrogel to optimize the mechanical properties of the mold. My results indicate that poly(AMPS) exhibits a rapid swelling and shrinking speed, enabling dynamic changes in object size (100%-350%). It also has satisfactory mechanical properties as a mold, either in the hydrated or dehydrated states, compared with the other two candidates. The poly(AMPS) mold has improved thermal stability with the decomposition temperature at 280°C, which opens possibilities for the preparation of various materials such as high-melting polymers or metals. It allows for dynamically resizing the infill material into various volumes based on needs.

4.3 Experimental details

4.3.1 Material formulation and preparation

4.3.1.1 Resin formulation

The resin formulation of poly(AMPS) was followed by our previous paper.[5,15] 136 mg 4-methoxyphenol (Alfa Aesar), 93.2 g 2-acrylamido-2-methyl-1-propanesulfonic acid (AMPS; Sigma-Aldrich), 62.06 mg quinoline yellow (Acros Organics), 10.8 g acrylamide (AAM, Fisher Scientific), and 3.8 g N, N'-methylenebisacrylamide (MBAA; Alfa Aesar) were added and mixed in 200 mL of dimethyl sulfoxide (DMSO; Fisher Scientific), followed by sonication until all chemicals were dissolved. 5.37 mL of ethyl (2,4,6-trimethylbenzoyl)phenylphosphinate (TPO-L; Oakwood Chemical) was added in the last step, then the bottle was sonicated until thoroughly mixed.

Poly(3-sulfopropyl acrylate potassium salt) (Poly(SPA)) and poly(acrylic acid) (poly(AA)) resins were prepared using the same method mentioned above. The only difference is that AMPS has been substituted with 65.25 g of 3-sulfopropyl acrylate potassium salt (SPA, 99%, Sigma-Aldrich) and 32.4 g of acrylic acid (AA, 99%, anhydrous, Sigma-Aldrich) monomer.

4.3.1.2 DLP printing

All printing was performed on a DLP printer (Elegoo Mars 3) with a UV wavelength of 405 nm. All structures used in this work were designed using Autodesk Inventor. The exposure time was optimized and set for each resin due to its different chemical environments: SPA, 10 sec; AMPS, 9 sec; and PAA, 20 sec. After printing, all samples were washed and soaked in isopropanol for 6 hours with fresh solutions being changed frequently to exchange the DMSO.

4.3.1.3 Cation solution soaking

1 M $CaCl_2$, 1 M NaCl, and 1 M HCl (control group) solutions were prepared for each print. Samples were soaked in each solution for 2 days. All samples were dried in the air overnight, followed by further drying in the 60°C vacuum oven for at least 5 hrs.

4.3.1.4 Infill material injection

All polymer-based infills were mixed in a mixer, "Thinky," for 4 minutes, followed by a 30-second degassing step. The mixture was then transferred into a 3 mL syringe. Pure metals were directly melted in the oven and loaded into the syringe. The infill materials were slowly pushed into the pre-processed mold. After curing or solidification, the filled mold was immersed in water to allow the outer mold to swell. The outer shell was gently peeled off with a razor.

4.3.2 Material characterizations

4.3.2.1 Thermal properties test

Thermogravimetric Analysis (TGA) tests were performed on a TGA Q50 instrument (TA Instruments, USA) equipped with software version V6.7 Build 203. Samples (~5–20 mg) were heated from 20°C to 500°C at a rate of 20°C/min under a protective nitrogen atmosphere (20 mL/min). Mass losses were recorded throughout the heating process.

4.3.2.2 Scanning Electron Microscopy (SEM)

The morphology of the printed samples was observed using a Scanning Electron Microscope (Zeiss Gemini 500, ZEISS Company, Germany). Samples were directly glued onto the SEM pin mount. An accelerating voltage of 3 kV was used. For high-magnification images, the "in-lens" mode was selected due to its high resolution.

4.3.2.3 "Hydrate" state mechanical test

Due to the fragile nature of the hydrate state sample, all mechanical tests were conducted on an Anton Paar MCR 301 rotational rheometer. A "compression" mode was used to test the strain-stress behaviors of the material. A fixed compression rate of 10 μm/s was applied to all tests. A flat hydrogel sample was cut into a ~10 mm × 5 mm × 4 mm size and placed onto the rheometer's lower plate. Each test was repeated at least three times to ensure reliability.

4.3.2.4 "Dehydrate" state mechanical test

The mechanical properties of the dehydrated sample were tested through nanoindentation. Nanoindentation was performed using an Anton Paar Hit 300 nanoindentation tester coupled with "Indentation 10.0.13" software to perform the measurements and calculations. A Berkovich tip was used for all nanoindentation measurements, along with identical experimental parameters as seen in Table S1. A sample of fused silica was indented prior to the measurement of samples to ensure instrument parameters were within the accepted ranges of the operational qualification values. Following each sample measurement, the tip was cleaned with isopropyl alcohol, followed by the indentation of a copper sample. Young's modulus was calculated from the reduced elastic modulus; this is due to elastic deformation occurring in the indenter and the sample, as shown by equation 1:

$$E_r = \frac{S\sqrt{\Pi}}{2\beta\sqrt{A_P}} \quad (1)$$

where E_r is the reduced Young's modulus, S is stiffness, β is a constant depending on the indenter shape, and A_p is the contact area.[17] The reduced Young's modulus is then converted to the indentation modulus, which is comparable with the Young's modulus of a given sample by:

$$E_{IT} = \frac{1-(\nu_s{}^2)}{\frac{1}{E_r}-\frac{1-(\nu_i{}^2)}{E_i}} \quad (2)$$

where E_{IT} is the indentation modulus, ν_s is the Poisson ratio of the sample, ν_i is the Poisson ratio of the indenter, and Ei is the Young's modulus of the indenter.[17,18]

Each sample was embedded into epoxy resin and polished down using 180 grit silicon carbide sandpaper using a LECO PX300 polishing station. Each sample was polished for 30 seconds with isopropyl alcohol until the samples were exposed and the resin was flat. The samples were placed into a vacuum furnace set to 60°C and vacuumed to 200 mbar for 16 hours. The samples were then slowly cooled to room temperature for 2 hours before performing nanoindentation measurements.

4.4 Results and discussion

4.4.1 Water absorbent material selections for adaptive mold

To prepare such an adaptive and transformable mold, I was looking for a water-absorbent material as the backbone, as it could intake a large amount of water and experience a significant volume change, just like a pufferfish. Therefore, I chose AMPS, SPA, and AA as the monomers for exploration; all of them are absorbent materials, while AMPS and SPA have been considered as super absorbent. Resin formulation was followed by our previous work with AAM as the co-monomer, MBAA as the crosslinker, and Na-TPO as the photoinitiator (Figure 4.4.1.1). Printing conditions were optimized for each resin. The preparation scheme is also shown in Figure 4.4.1.1. I set three key parameters as the primary criteria for evaluating the success of the desirable molds: fast and significant expansion and shrinkage behaviors, good mechanical properties, and superior thermal stability. Therefore, measurements were conducted, and results were discussed as follows.

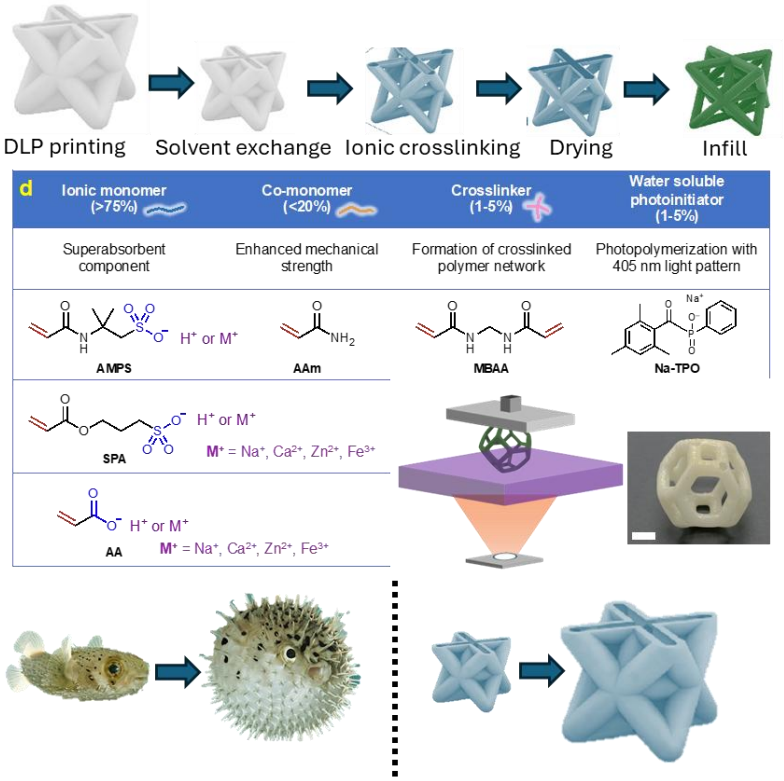

Figure 4.4.1.1 Preparation scheme of adaptive mold and material composition of the resin used for printing the mold.

I first examined the transformable behaviors to compare which hydrogel best mimics the blowing process of pufferfish. In Figure 4.4.1.2 (a), the volume expansion and shrinkage of those three hydrogels are shown. Instead of using DI water as the swelling agent, 1 M $CaCl_2$ was chosen for two purposes: 1) Crosslinking the hydrogel to maintain a satisfactory modulus in the hydrated state to sustain the pressure from infill injection. 2) Slowing down the rate of expansion to make it more controllable, as rapid expansion may lead to uneven stress distribution, which could lead to a rupture. After samples reached their maximum volumes, they were soaked in IPA to facilitate the expulsion of the water for faster dehydration. In Figure 4.4.1.2 (a), poly(SPA) and poly(AMPS) exhibit rapid expansion rates, increasing 5 times and 3 times, respectively, within 20 minutes. As a regular absorbent material, PAA not only has a slow swelling rate (1.1x within 20 mins) but also scored the minimal peak expansion (125% vs. 796%, 351%). The maximum volumetric expansion is a key indicator since it constrains the range of expansion; higher expansion volume would enable greater size tunability of the printed mold. Therefore, both poly(SPA) and poly(AMPS) are promising candidates in terms of potential adaptive behaviors.

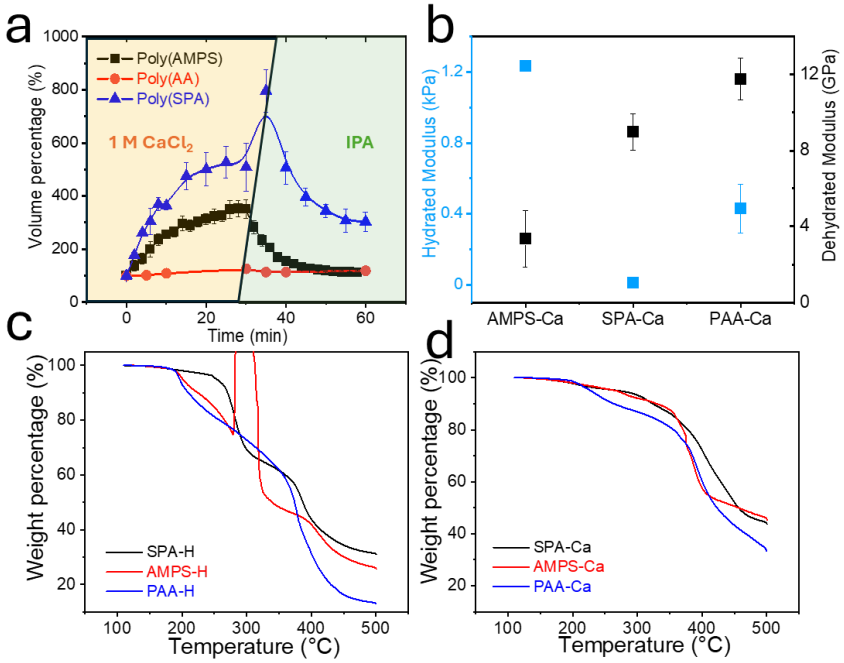

Figure 4.4.1.2. (a) Swelling and shrinking behaviors of the three hydrogels. (b) Mechanical properties of the three crosslinked hydrogels. (c) TGA of the un-crosslinked hydrogels. (d) TGA of the crosslinked hydrogels.

The mechanical properties of those hydrogels are important because the printed mold needs to maintain necessary integrity, either in the dehydrated or hydrated states. To quantify this, I carried out the mechanical test for the dehydrated and hydrated samples separately, and the moduli are shown in Figure 4.4.1.2 (b). All three samples exhibited modulus in the gigapascal (GPa) range when completely dried out, suggesting they are able to act as a rigid mold in this condition. In the fully hydrated state, all hydrogels experienced a dramatic decrease in stiffness, and the poly(SPA)

is the most vulnerable to failure, with a modulus of only 11.5 Pa. It can barely afford its self-weight in this case, therefore preventing this polymer from being a functional mold.

Thermal stability was characterized by TGA on all three dried hydrogel samples. Higher decomposition temperature would enable the mold to withstand the processing of high-temperature melts, thus unlocking a wider range of material selections. TGA curves are shown in Figures 4.4.1.2 (c) and (d). Without crosslinking, poly(SPA) started to decompose at 246°C while PAA and poly(AMPS) decomposed at 189°C. The side chain and amide group on the backbone may impair the thermal stability of poly(AMPS) when compared with poly(SPA), and the carboxylic acid groups on PAA were considered as the primary cause of the inferior thermal stability. The data shows that the ionic crosslinking effectively enhanced the stability of all samples. The decomposition temperature of poly(AMPS) increased to 275°C, which is comparable to that of poly(SPA) of 297°C. PAA reached 206°C and then started to degrade from this temperature.

Considering the expansion and shrinkage behaviors, mechanical properties, and thermal stability together, poly(AMPS) has the most balanced properties. Therefore, poly(AMPS) was selected as the mold material from this point onward.

4.4.2 Ion species influence on poly(AMPS)

My previous results show that Ca^{2+} contributes to crosslinking the hydrogel, thereby increasing the thermal stability of poly(AMPS). I was also curious about how the ion species would influence the material properties. To investigate this, I prepared a group of printed poly(AMPS) and soaked them in 1 M NaCl solutions (poly(AMPS-Na)) to compare them with samples soaked in 1 M HCl (poly(AMPS-H)) and 1 M $CaCl_2$ (poly(AMPS-Ca)).

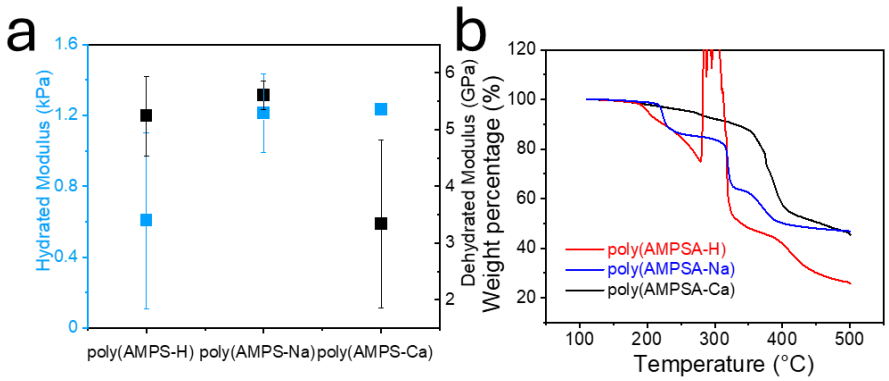

Figure 4.4.2 (a) Mechanical properties of different ion species crosslinked poly(AMPS). (b) Thermal stability of different ion species crosslinked poly(AMPS).

Unsurprisingly, in Figure 4.4.2 (a), both Na^+ and Ca^{2+} increased the modulus of hydrate samples through crosslinking, but the bivalence of Ca^{2+} did not seem to make a significant difference, as the moduli of those two are very close. A more pronounced change is observed in Figure 4.4.2 (b) that Ca^{2+} crosslinked hydrogel has a higher decomposition temperature at 275°C compared to that of Na^+ crosslinked hydrogel at 215°C. This suggests that the Ca cation may lead to a higher degree of crosslinking, but its influence on mechanical properties may not be as noticeable as the degradation temperature. However, I need to point out that, even though the previous two results corroborate each other, the nanoindentation results of poly(AMPS-Ca) are an outlier as it is even softer than poly(AMPS-Na). I do not have a very good explanation at the

moment. This inconsistency could be the result of the intrinsic drawbacks of nanoindentation measurements that only reflect the surface stiffness of bulk materials.

4.4.3 Effect of drying methods on mold property

In my previous study, I used IPA to achieve a rapid solvent exchange, mimicking the pufferfish's expulsion of swallowed water. However, it remains unclear whether this faster drying method alters any material properties. To explore the effect of the drying method on material properties, I air-dried another group of poly(AMPS) as a control group.

In Figure 4.4.3 (a), the "onset" of degradation of the fast drying sample quickly drops to 175°C. A significant degradation rate change was observed in this curve; the sample experienced a rapid decomposition with a narrow window between approximately 275 and 300°C. This decreased thermal stability implies that possible changes happened to the material structure. Hence, I performed SEM to observe the microstructure of fast-dried samples. Compared with the control group, which has a smooth and uniform surface, the fast-dried samples possess a porous microstructure (see Figure 4.4.3 (b) and (c)). This could be explained by the reason that the dehydration agent IPA is less polar than water, hence it is less favored by poly(AMPS). When depleting water inside the hydrogel, the soaked IPA caused the phase separation and then left the micropores. Those micropores make the poly(AMPS) more vulnerable to heat. These findings suggest IPA could successfully act as a dehydration agent to expel water, but at the cost of sacrificing thermal stability. When preparing the mold, we need to pay extra attention to the drying process according to the properties of our intended infill materials. However, it is interesting that poly(SPA) exhibits behaviors that are inconsistent with those of poly(AMPS). In Figures 4.4.3 (e) and (f), the slow air-dry process left dense micropores inside poly(SPA) while the fast solvent exchange led to a relatively smooth surface. As a consequence, fast-dried samples have better thermal stability (Figure 4.4.3 (d)). This reverse result between poly(AMPS) and poly(SPA) might be due to the difference in affinity to water and IPA. Poly(SPA) forms fewer hydrogen bonds with water; therefore, it favors less water but may be partially dissolved or swelled by IPA. Thus, the drying method should be chosen on a case-by-case basis.

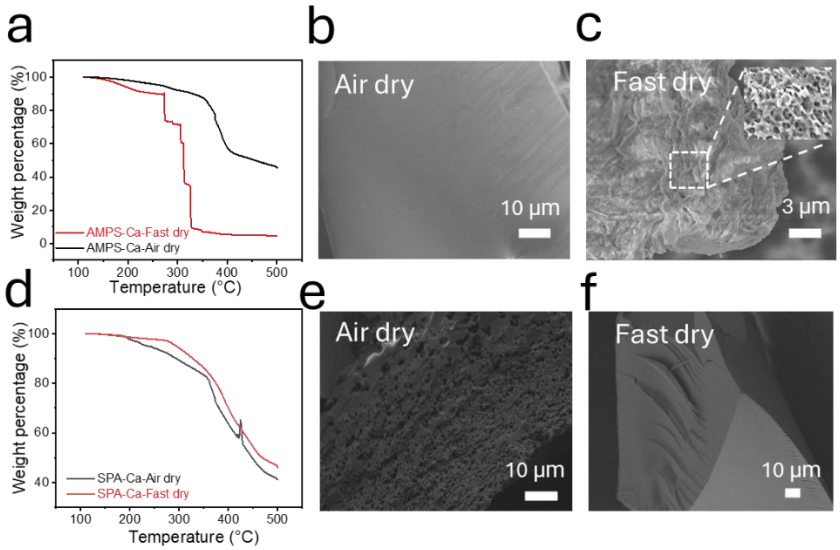

Figure 4.4.3 (a) TGA of Ca-crosslinked poly(AMPS) with different drying methods. (b) SEM image of air-dried poly(AMPS). (c) SEM image of air-dried poly(AMPS). (d) TGA of Ca-crosslinked

poly(SPA) with different drying methods. (e) SEM image of air-dried poly(SPA). (f) SEM image of air-dried poly(SPA).

4.4.4 Adaptive mold with tunable size and material injection

My poly(AMPS) hydrogel could be printed into various hollow structures (Figure 4.4.4 (a) to (d)). After ionic crosslinking and drying, I prepared four complex structures for demonstration: truncated octahedral, tetrahedral, octahedral lattice, and spring. This proves the versatility of designing and printing poly(AMPS) into various geometries. I later demonstrated material versatility by choosing three typical materials: Field's metal, polymer metal composites, and pure polymer to fill the hollow spring mold (Figure 4.4.4 (e)-(g)).

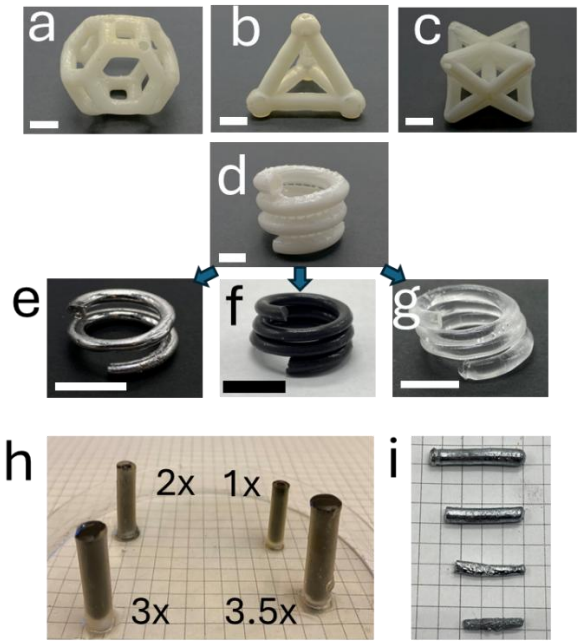

Figure 4.4.4 Images of (a) Truncated octahedral mold. (b) Tetrahedral mold. (c) Octahedral mold. (d) Spring mold. (e)-(f) Material casting through the spring mold. (e) Field's metal. (f) Iron particle/PDMS (1:1 weight ratio). (g) PDMS. (h) Adaptive mold with different-sized expansion. (i) Gallium casting through the adaptive mold in (h).

The adaptability and tunability of sizes are demonstrated by controlling the soaking time of the printed hollow beam mold in a $CaCl_2$ solution. Based on my previous study, I soaked separate beam molds in the metal cation solution for 5 minutes, 10 minutes, 15 minutes, and 25 minutes, which corresponded to 100%, 200%, 300%, and 350% volume percentage (Figure 4.4.4 (h)). I was able to inject liquid gallium into the mold and obtain beams at different expansion sizes after solidification (Figure 4.4.4 (i)).

4.5 Conclusion and outlooks

In this work, I investigated the key requirements to select the base material to be an adaptive DLP printed mold. I found that poly(AMPS) exhibits relatively fast expandable and shrinkage behaviors when soaked in a $CaCl_2$ and IPA solution, reaching a maximum volume percentage of 350%. It also shows relatively good thermal stability and mechanical stability in both hydrated and dehydrated states. My study reveals that the ion crosslinking will enhance both the thermal and mechanical stability, and the divalent cations have a more dominant influence on

thermal properties than single-charged cations. The drying method would also influence hydrogel properties, as the evaporation of solvent could lead to microstructure changes.

I demonstrated that the poly(AMPS) mold can successfully mimic the "bulking" behaviors of pufferfish, thereby allowing the mold to be actively controlled to different volumes. This work expands the library of materials that can be fabricated into high complexity and also offers a solution for achieving multi-size fabrication within a single adaptive mold.

4.6 References

(1) Abdulhameed, O.; Al-Ahmari, A.; Ameen, W.; Mian, S. H. Additive Manufacturing: Challenges, Trends, and Applications. *Adv. Mech. Eng.* **2019**, *11* (2), 1687814018822880. https://doi.org/10.1177/1687814018822880.

(2) Shahrubudin, N.; Lee, T. C.; Ramlan, R. An Overview on 3D Printing Technology: Technological, Materials, and Applications. *Procedia Manuf.* **2019**, *35*, 1286–1296. https://doi.org/10.1016/j.promfg.2019.06.089.

(3) Lee, J.-Y.; An, J.; Chua, C. K. Fundamentals and Applications of 3D Printing for Novel Materials. *Appl. Mater. Today* **2017**, *7*, 120–133. https://doi.org/10.1016/j.apmt.2017.02.004.

(4) Goodarzi Hosseinabadi, H.; Nieto, D.; Yousefinejad, A.; Fattel, H.; Ionov, L.; Miri, A. K. Ink Material Selection and Optical Design Considerations in DLP 3D Printing. *Appl. Mater. Today* **2023**, *30*, 101721. https://doi.org/10.1016/j.apmt.2022.101721.

(5) Jordan, R. S. 3D Printed Architected Conducting Polymer Hydrogels. *J Mater Chem B* **2021**, 13.

(6) Li, Y.; Li, C.; Zhang, X.; Wang, Y.; Tan, Y.; Chang, S.; Chen, Z.; Fu, G.; Kou, Z.; Stefan, A.; Xu, X.; Ding, J. Incorporating Metal Precursors towards a Library of High-Resolution Metal Parts by Stereolithography. *Appl. Mater. Today* **2022**, *29*, 101553. https://doi.org/10.1016/j.apmt.2022.101553.

(7) Varghese, G.; Moral, M.; Castro-García, M.; López-López, J. J.; Marín-Rueda, J. R.; Yagüe-Alcaraz, V.; Hernández-Afonso, L.; Ruiz-Morales, J. C.; Canales-Vázquez, J. Fabrication and Characterisation of Ceramics via Low-Cost DLP 3D Printing. *Bol. Soc. Esp. Cerámica Vidr.* **2018**, *57* (1), 9–18. https://doi.org/10.1016/j.bsecv.2017.09.004.

(8) Martinelli, A.; Nitti, A.; Giannotta, G.; Po, R.; Pasini, D. 3D Printing of Conductive Organic Polymers: Challenges and Opportunities towards Dynamic and Electrically Responsive Materials. *Mater. Today Chem.* **2022**, *26*, 101135. https://doi.org/10.1016/j.mtchem.2022.101135.

(9) Ryan, K. R.; Down, M. P.; Hurst, N. J.; Keefe, E. M.; Banks, C. E. Additive Manufacturing (3D Printing) of Electrically Conductive Polymers and Polymer Nanocomposites and Their Applications. *eScience* **2022**, *2* (4), 365–381. https://doi.org/10.1016/j.esci.2022.07.003.

(10) Jordan, R. S.; Wang, Y. 3D Printing of Conjugated Polymers. *J. Polym. Sci. Part B Polym. Phys.* **2019**, *57* (23), 1592–1605. https://doi.org/10.1002/polb.24893.

(11) Ruiz-Mateos Serrano, R.; Aguzin, A.; Mitoudi-Vagourdi, E.; Tao, X.; Naegele, T. E.; Jin, A. T.; Lopez-Larrea, N.; Picchio, M. L.; Vinicio Alban-Paccha, M.; Minari, R. J.; Mecerreyes, D.; Dominguez-Alfaro, A.; Malliaras, G. G. 3D Printed PEDOT: PSS-Based Conducting and Patternable Eutectogel Electrodes for Machine Learning on Textiles. *Biomaterials* **2024**, *310*, 122624. https://doi.org/10.1016/j.biomaterials.2024.122624.

(12) Song, C.; Zhao, Q.; Xie, T.; Wu, J. DLP 3D Printing of Electrically Conductive Hybrid Hydrogels *via* Polymerization-Induced Phase Separation and Subsequent *in Situ* Assembly of Polypyrrole. *J. Mater. Chem. A* **2024**, *12* (9), 5348–5356. https://doi.org/10.1039/D3TA06779C.

(13) Lopez-Larrea, N.; Criado-Gonzalez, M.; Dominguez-Alfaro, A.; Alegret, N.; Agua, I. D.; Marchiori, B.; Mecerreyes, D. Digital Light 3D Printing of PEDOT-Based Photopolymerizable Inks for Biosensing. *ACS Appl. Polym. Mater.* **2022**, *4* (9), 6749–6759. https://doi.org/10.1021/acsapm.2c01170.
(14) Saccone, M. A.; Gallivan, R. A.; Narita, K.; Yee, D. W.; Greer, J. R. Additive Manufacturing of Micro-Architected Metals via Hydrogel Infusion. *Nature* **2022**, *612* (7941), 685–690. https://doi.org/10.1038/s41586-022-05433-2.
(15) Hill, I. M., Xu, B., Rosenberg, A. A., Chang, J., Wu, D., Rice, W., Tran, E., Gutierrez, L., Rubin, Y., Yeung, M. T., Wang, Y. 3D-Printing Assisted Casting of Pure PEDOT with Complex Architectures. (in preparation)
(16) Wainwright, P. C.; Turingan, R. G. EVOLUTION OF PUFFERFISH INFLATION BEHAVIOR. *Evolution* **1997**, *51* (2), 506–518. https://doi.org/10.1111/j.1558-5646.1997.tb02438.x.
(17) Oliver, W. C.; Pharr, G. M. An Improved Technique for Determining Hardness and Elastic Modulus Using Load and Displacement Sensing Indentation Experiments. *J. Mater. Res.* **1992**, *7* (6), 1564–1583. https://doi.org/10.1557/JMR.1992.1564.
(18) MA, D.; Chung Wo, O.; Liu, J.; HE, J. Determination of Young's Modulus by Nanoindentation. *Sci. China Ser. E Technol. Sci.* **2004**, *47* (4), 398–408. https://doi.org/10.1360/03ye0590.

Chapter 5
Conclusion and outlooks

In my PhD work, I explored using living organisms as inspiration to manufacture adaptive materials. Specifically, in Chapter 1, my work explored a way to build a transformative material with a nacre-like structure to endow the transformative material with high toughness. This method provides a route to combine biometric features within one sole entity, namely, in this case, the transformative "Soft/Hard" transition of sea cucumber and the high toughness of nacre. This work offers three useful insights into designing such transformative and tough material: 1) The overlapping pattern should be designed to favor a high probability of deflection/penetration. 2) Structural parameters should be optimized on a case-by-case basis for different material systems. 3) Large numbers of nacre layers are beneficial for toughening the composites. In Chapter 2, I came up with a new strategy to replicate the "J-shape" adaptive behaviors of biomaterials. My goal was successfully achieved by harnessing the squeezing behaviors of MRF. My investigation also showed that the "J-shape" curve could be tuned by segmentation and manual activation. Integrating with 3D structures allows the MRF to be further programmed and endows MRFs with multiple-level responses. In Chapter 3, inspired by the "bulking" behaviors of pufferfish, I explored using superabsorbent hydrogels to mimic that ability. Poly(AMPS) exhibits fast swelling and shrinking behaviors that allow for dynamic control of the size of the DLP-printed molds. These molds enlarge the library of materials that could be used in the casting method.

With the advancement of recent progress in artificial intelligence (AI), robotics with advanced algorithms could reason, think, and behave more like human beings. However, existing traditional materials with fixed properties or functionalities will not satisfy the fast-changing environments. To catch up with the development of AI and robotics, materials need to be developed from responsive to adaptive or even intelligent. This work paves the way for future adaptive or intelligent matters. The three bioinspired synthetic materials with adaptive behaviors present in this dissertation could serve as a platform for future transformative electronics, armors, or robots. Most importantly, my results point out that nature could be a resourceful and inexhaustible library of inspirations for designing future artificial materials. Directly learning from living organisms could be a "shortcut" for us to borrow the ideas that nature has taken millions of years to develop.

At the same time, I recognize that all those bioinspired adaptive materials I demonstrated are still in their infancy for the following reasons: 1) The current bioinspired design has not fully replicated all the features of natural adaptive materials. For example, though transformative behaviors have been successfully achieved, the transition of my sea cucumber-like material is not as fast as a real sea cucumber, and my nacre-like structure has not replicated the micro- or nano-scale features like tablet interlocking, nano-asperity on the tablet, and adhesive organic interface. 2) My adaptive materials are not equipped with computing units; therefore, all adaptive behaviors are pre-designed and programmed by humans. They lack the ability to process the information independently and determine the corresponding responses, especially when the environment shifts out of their scope. The absence of computing units also prohibits the evolution of adaptive materials; as a consequence, my adaptive materials retain the same characteristics no matter how the outer world changes. 3) Unlike natural adaptive matter that has been used for millions of years, the long-term stability of my synthetic material remains to be systematically validated. Some of my material systems adopt liquid-solid composites, but the intrinsic drawback that liquid is not compressible still poses challenges for the long run.

Future work may focus on addressing the above-mentioned challenges. Further investigations into the adaptive behaviors of organisms in nature. A deeper understanding of existing adaptive organisms will provide more inspiration for future designs. Meanwhile, material systems with superior stability and better biocompatibility should be prepared for adaptive materials. New manufacturing techniques are also indispensable for their development. Our past experience has shown that 3D printing technology profoundly influences the manufacturing of new materials, allowing us to prepare those materials with greater complexity. I anticipate that the coming of future bioinspired adaptive materials will rely heavily on the new materials and manufacturing technologies.

To move forward to make our current adaptive material more intelligent, an information processing and computing "brain" is highly desirable for such a material system. Recent attempts have been made to integrate liquid crystal elastomer with organic neuromorphic systems. The neuromorphic computing devices offer basic neural network calculation ability to the adaptive material, thus helping it to make decisions based on different external stimuli. I foresee that the neuromorphic devices will play a more critical role in decision making, material evolution, and intelligent behaviors of adaptive materials. Another possible route is to connect the adaptive materials with living creatures. It could either be physically attached to the living organisms or just stay in the same chemical medium. Future studies could fully use biochemicals secreted by living things as the stimulus, like neurotransmitters, to trigger transitions.

Collectively, this dissertation reflects an ongoing pursuit of understanding and mimicking the adaptive behaviors of nature. This research serves as a step toward the development of more adaptive and intelligent synthetic matter.